Article

24.8%-efficient planar perovskite solar cells via ligand-engineered TiO$_2$ deposition

The ligand-engineered deposition (LD) strategy based on the coordination ability of ligands (such as tartaric acid) is proposed to regulate TiO$_2$ film and interfacial structure. The resultant planar perovskite solar cells (PSCs) achieve an impressive PCE of 24.8% with a fill factor exceeding 0.83, which is the highest PCE among the TiO$_2$-based planar PSCs reported so far.

Hao Huang, Peng Cui, Yan Chen, ..., Xin Wang, Xunlei Ding, Meicheng Li

mcli@ncepu.edu.cn

Highlights

A ligand-engineered deposition strategy to regulate TiO$_2$ ETL formation dynamic

24.81% efficiency is achieved for TiO$_2$-based planar PSCs

>0.83 FF is achieved due to the optimized TiO$_2$ and interfacial structure

An extensional reference of ligand-engineered deposition strategy for efficient PSCs

Article

24.8%-efficient planar perovskite solar cells via ligand-engineered TiO$_2$ deposition

Hao Huang,[1,3] Peng Cui,[1,3] Yan Chen,[2] Luyao Yan,[1] Xiaopeng Yue,[1] Shujie Qu,[1] Xinxin Wang,[1] Shuxian Du,[1] Benyu Liu,[1] Qiang Zhang,[1] Zhineng Lan,[1] Yingying Yang,[1] Jun Ji,[1] Xing Zhao,[1] Yingfeng Li,[1] Xin Wang,[2] Xunlei Ding,[2] and Meicheng Li[1,4,*]

SUMMARY

Planar perovskite solar cells (PSCs) have been extensively researched as a promising photovoltaic technology, wherein the electron extraction and transfer play a crucial role in the power conversion efficiency (PCE). Here, we proposed a ligand-engineered deposition strategy based on the coordination ability of ligands (e.g., tartaric acid) to regulate TiO$_2$ film and interfacial structure. This strategy can effectively inhibit particle aggregation of TiO$_2$ film through the steric hindrance of assembled ligands. Furthermore, the decreased interfacial contact impedance and enhanced electron extraction are achieved between TiO$_2$ and perovskite, due to the smooth topography and cross-linked structure formed by tartaric acid that bonds with Ti and Pb atoms. Accordingly, an impressive PCE of 24.8% with a fill factor exceeding 0.83 is successfully obtained, which is the highest PCE among TiO$_2$-based planar PSCs reported so far. In addition, unencapsulated PSCs can maintain ∼95% of initial efficiency upon exposure to ambient air for 2,000 h.

INTRODUCTION

Metal halide perovskite solar cells (PSCs) have been considered as a promising technology for solar energy capture and conversion owing to their high-efficiency and low-cost solution preparation. Compared with the mesoporous-structured PSCs that include a scaffold layer, the planar PSCs have the advantages of simple construction, easy and low-temperature fabrication, showing outstanding potential in tandem solar cells and flexible application.[1–3] In the planar PSCs, the electron transport layers (ETLs) such as TiO$_2$, SnO$_2$, and ZnO have been intensively researched for their excellent photoelectric properties.[4–6] Encouragingly, through the carrier management, the planar PSCs with SnO$_2$ have achieved certificated power conversion efficiency (PCE) over 25%,[7,8] which demonstrates their high-efficiency potential. However, for TiO$_2$ material that is more inexpensive and reserved-abundant than SnO$_2$, the certificated PCE of corresponding planar PSCs still stagnates under 24%, far below the Shockley-Queisser (S-Q) limit.[9] The reason for this inferior performance should be related to the low-quality of TiO$_2$ film and its poor interfacial contact with perovskite film, which plays a crucial part in the electron transport within planar PSCs.[10,11] Therefore, to improve the PCE of planar PSCs with TiO$_2$, it is a feasible approach to simultaneously modulate the TiO$_2$ and its interfacial contact property through precisely controlled TiO$_2$ deposition.

To obtain a high-quality TiO$_2$ film, various deposition methods have been carried out.[12–14] Among them, spin-coating is one of the most common methods owing

CONTEXT & SCALE

Perovskite solar cells (PSCs) have been intensively researched as a promising photovoltaic technology due to their high efficiency and low-cost fabrication. In the planar PSCs, which show outstanding potential in tandem solar cells and flexible application, the quality of the electron transport layer (ETL) plays a crucial role in the power conversion efficiency (PCE). Herein, we proposed a ligand-engineered deposition strategy based on the coordination ability of ligands (such as tartaric acid) to regulate TiO$_2$ ETL and interfacial structure. Owing to the inhibited particle aggregation, decreased ETL/perovskite interfacial contact impedance and enhanced electron extraction, the planar resultant PSCs exhibit a PCE of 24.8% (certified 24.5%), the highest among TiO$_2$-based planar PSCs reported so far. This ligand-engineered deposition strategy provides a new approach to improve the performance of planar PSCs, which helps to push forward their further development.

to its simple operation. As early as 2017, based on the spin-coating method, a solvent strategy that employed methanol and chloroform as TiO_2 precursor solvents was proposed to fabricate chlorine-capped TiO_2 colloidal nanocrystal film, resulting in a PCE of 21.4%.[15] To further improve TiO_2 film property and realize environmentally friendly application, Gao et al.[16] used water as TiO_2 nanocrystal solvent and performed alkali metal chloride doping strategies, promoting the PCE of planar PSCs up to 23.1%. Except for the spin-coating, the atom layer deposition, magnetron sputtering, e-beam evaporation, and chemical bath deposition have been also proposed to obtain the TiO_2 film on fluorine-doped tin oxide (FTO) substrate. Compared with atom layer deposition and magnetron sputtering that need expensive instruments and high processing temperature, the chemical bath deposition can realize low-temperature and conformal film forming, which is suitable for the substrate such as FTO with micro-structured surface. In 2020, Liu et al. applied chemical bath deposited TiO_2 as ETL, achieving a PCE of planar PSCs up to 23.25%,[17] and the PCE was further promoted to 23.4% in the next year.[18] Although combining the crystallization regulation strategy and surface modification strategy on TiO_2 fabricated with chemical bath deposition achieved a certificated PCE of 23.7%,[9] which still leaves much room for further improvement. During the TiO_2 chemical bath deposition process, the violent hydrolysis reaction and active intermediate products will produce large agglomerated particles and oxygen vacancy, leading to an inferior TiO_2 film topography and TiO_2/perovskite interfacial contact property, restricting the PCE improvement of planar PSCs.[19] Hence, it is necessary to develop a regulation strategy of TiO_2 chemical bath deposition to obtain excellently applicable ETL for efficient planar PSCs.

To precisely control the deposition process, effective methods to introduce the ligands that can coordinate with the transition metal atoms into the precursor were researched. Wang et al. reported a surface ligand management for obtaining high-quality $CsPbI_3$ perovskite quantum dots. Through introducing di-n-propylamine (DPA), the defect states of nanocrystal were effectively reduced, approaching 15% for $CsPbI_3$ quantum dot-based solar cell.[20] Except for passivating the defects, the ligands can also serve as block-copolymer or steric hinder to regulate the deposition process of a film composed of multiple nanoparticles.[21] Therefore, it is supposed to be a significant progress in TiO_2 deposition by using the ligand-engineered strategy.

Herein, we proposed a ligand-engineered deposition (LD) strategy to precisely regulate the TiO_2 deposition process using the additive ligands such as tartaric acid (TA), ethylene diamine tetraacetic acid (EDTA), phenylphosphonic acid (PA), and so on. The regulated TiO_2 film (LD-TiO_2) exhibits reduced particle aggregation and improved electron mobility compared with the control sample. Furthermore, the LD-TiO_2/perovskite interface contact property has also been effectively optimized, leading to a decreased contact impedance and enhanced electron extraction. As a result, high-efficiency planar PSCs with LD-TiO_2 have been fabricated, achieving a PCE of 24.81% (certificated 24.5%), the highest value among the reported TiO_2-based planar PSCs so far. In addition, both the ultraviolet (UV) and humidity stabilities of TiO_2-based PSCs have been effectively enhanced.

RESULTS AND DISCUSSION
The LD mechanism and optimized TiO_2 film
It is well known that the TA can coordinate with transition metal oxide to form a complex through its lone-pair electrons of carboxyl group moving to the vacant orbitals

[1]State Key Laboratory of Alternate Electrical Power System with Renewable Energy Sources, School of New Energy, North China Electric Power University, Beijing 102206, China

[2]Institute of Clusters and Low Dimensional Nanomaterials, School of Mathematics and Physics, North China Electric Power University, Beijing 102206, China

[3]These authors contributed equally

[4]Lead contact

*Correspondence: mcli@ncepu.edu.cn
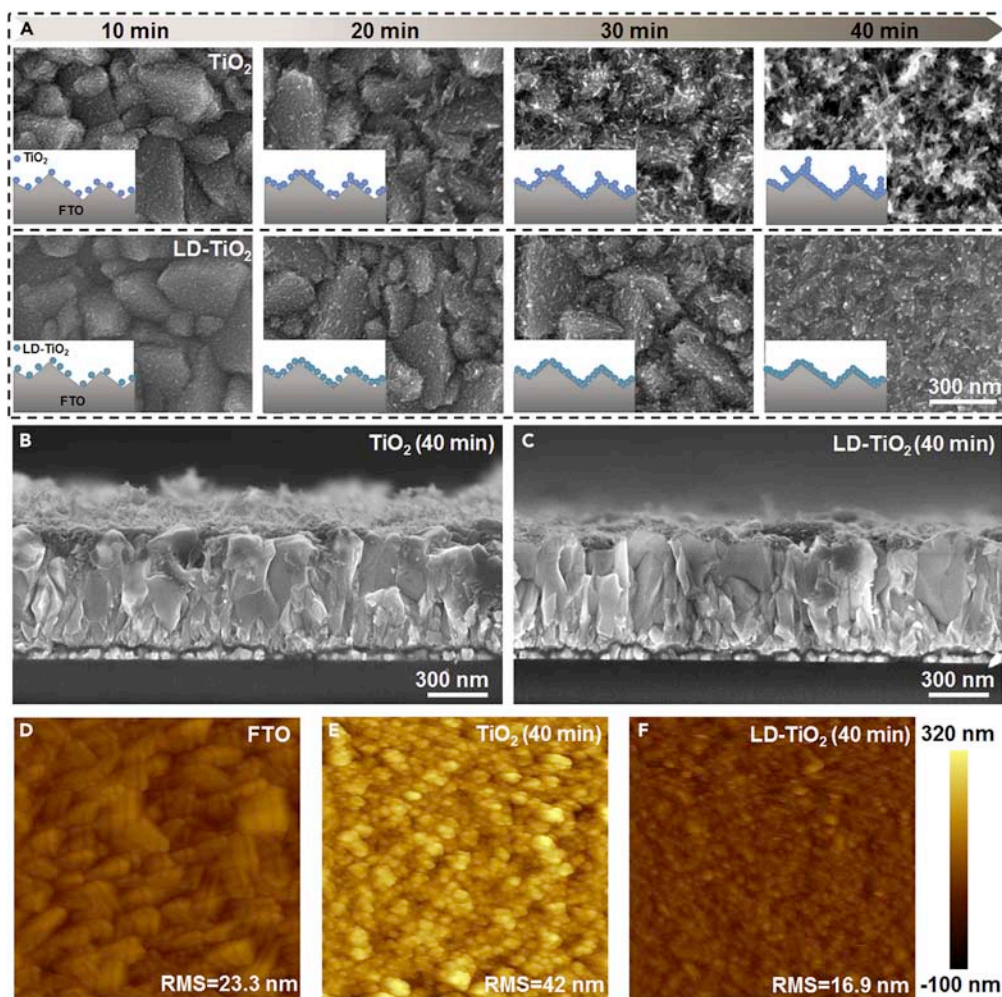
Figure 1. Topography evolution with deposition time of TiO$_2$ films that are deposited on FTO
(A) SEM images of TiO$_2$ film and LD-TiO$_2$ film with different bath times, and the deposition schematics are included in the inset.
(B and C) Cross-sectional SEM images of TiO$_2$ film and LD-TiO$_2$ film.
(D–F) AFM images of FTO, TiO$_2$ film, and LD-TiO$_2$ film, the graph size is 2.5 × 2.5 µm.

of transition metal atom.[22,23] Thus, the TA (chemical structure shown in Figure S1) was chosen as the ligands in TiO$_2$ chemical bath deposition. We introduced TA into the deionized water, and then the complex reacted with titanium tetrachloride (TiCl$_4$) to prepare the chemical bath precursor. The bath time of immersed substrate was 40 min, according to the previous reports,[4] and the introduced amount of TA was 0.3 mmol (the molar ratio of TA/TiCl$_4$ is 1.05%). To systematically explore the influence of LD strategy on TiO$_2$ film topography, we carried out the scanning electron microscope (SEM) to observe TiO$_2$ and LD-TiO$_2$ with different bath times. As shown in Figure 1A, after 10 min deposition, both the TiO$_2$ and LD-TiO$_2$ nanoparticles begin to land on the surface of FTO. As the bath time increases to 20 min, we can observe the growth of deposited TiO$_2$ and LD-TiO$_2$ nanoparticles, and the continuous film begins to form. However, it is worth noting that the TiO$_2$ nanoparticles begin to agglomerate in this stage, which is supposed to further impact TiO$_2$ film topography in the following deposition process. When the bath time is 30 min, the TiO$_2$ and LD-TiO$_2$ film can be obviously observed. Meanwhile, the agglomeration phenomenon is also found to be more severe in the TiO$_2$ film. In

comparison, the agglomeration has not occurred in the LD-TiO$_2$ film, indicating that the introduced ligands improve film uniformity. The LD-TiO$_2$ film surface is still smooth and compact with complete coverage until the deposition time comes to 40 min. However, the TiO$_2$ film yields a rough and crackled surface with large clusters and protrusion in this stage, just like the seabed-covered coral tree. From the illustration, we can be more conscious of the difference between the TiO$_2$ and LD-TiO$_2$ topography, gaining an insight into the inhibition of LD strategy on nanoparticle agglomeration and enormous-cluster formation.

To understand the mechanism of LD strategy and its influence on the TiO$_2$ film topography, the chemical bath deposition process was analyzed. There are three stages: (1) hydrolysis and nucleation, TiCl$_4$ hydrolysis and titanium ions in the solution are bonded together to form crystal nucleus; (2) growth of crystal nucleus, continuous enlarging crystal nucleus forms nanocrystal, which precipitates in the solution, and the color of the solution becomes milk white; (3) crystal particle deposition, the suspended nanocrystals are attracted to each other become crystal particles by electrostatic force, and then crystal particles deposit on the substrate with the free energy reduction. During the chemical bath deposition, the electronic property and microstructure of TiO$_2$ film are closely related to the reactivity of the transitional species and the crystal particle deposition process. With applied LD strategy (Figure S2), the transitional species reactivity is effectively reduced through TA bonding with titanium and forming the assembled complex, which retards the generation of particle agglomeration and oxygen vacancy. In the deposition process, the falling TiO$_2$ crystal is prone to generate aggregation through the electrostatic, leading to a rough and uneven TiO$_2$ topography. In comparison, the LD-TiO$_2$ crystal particles can uniformly deposit on the substrate due to the electrostatic repulsion and steric hindrance of assembled TA ligands, which results in a smooth and compact LD-TiO$_2$ film. The cross-sectional SEM images of TiO$_2$ film (Figure 1B) show that the large cluster and protrusion that looks like a coral tree be clearly observed in the TiO$_2$ film. However, the LD-TiO$_2$ film (Figure 1C) exhibits a compact and smooth topography, confirming the inhibition of the LD strategy on the aggregation.

The atomic force microscope (AFM) was carried out to further characterize the topography and quantify the surface roughness of TiO$_2$ film and LD-TiO$_2$ film. To comprehensively understand the influence of LD strategy on the TiO$_2$ deposition process, the surface topography of FTO was also researched (Figure 1D). The RMS of FTO is 23.3 nm, and the observed topography of FTO is consistence with the SEM results shown in Figure 1A, where we can observe the FTO surface. It is observed that there are large protrusions and aggregations in the TiO$_2$ film (Figure 1E), which is in agreement with the SEM images shown in Figure S3. The RMS of TiO$_2$ film is 42 nm, which is obviously larger than that of FTO. As shown in Figure 1F, the RMS of LD-TiO$_2$ film is 16.9 nm, which is even smaller than that of FTO, indicating the controlled deposition process with LD strategy.

To confirm the existence of TA in TiO$_2$ film and gain an insight into its chemical states, X-ray photoelectron spectroscopy (XPS) was carried out. The high-resolution spectra of the C and O elements selected from the full spectra (Figure S4A) are shown in Figures 2A and 2B. Compared with the C 1s spectrum of TiO$_2$, it is obviously observed a new peak located at 288.7 eV that denotes the C=O group of TA in the C 1s spectrum of LD-TiO$_2$.[24–26] After deconvoluting the O 1s peak of LD-TiO$_2$ into three peaks located at 530 eV (O–Ti), 531.4 eV (O–H),[27,28] and 532.2 eV (C=O),[29] respectively, we can clearly observe the appearance of C=O peak
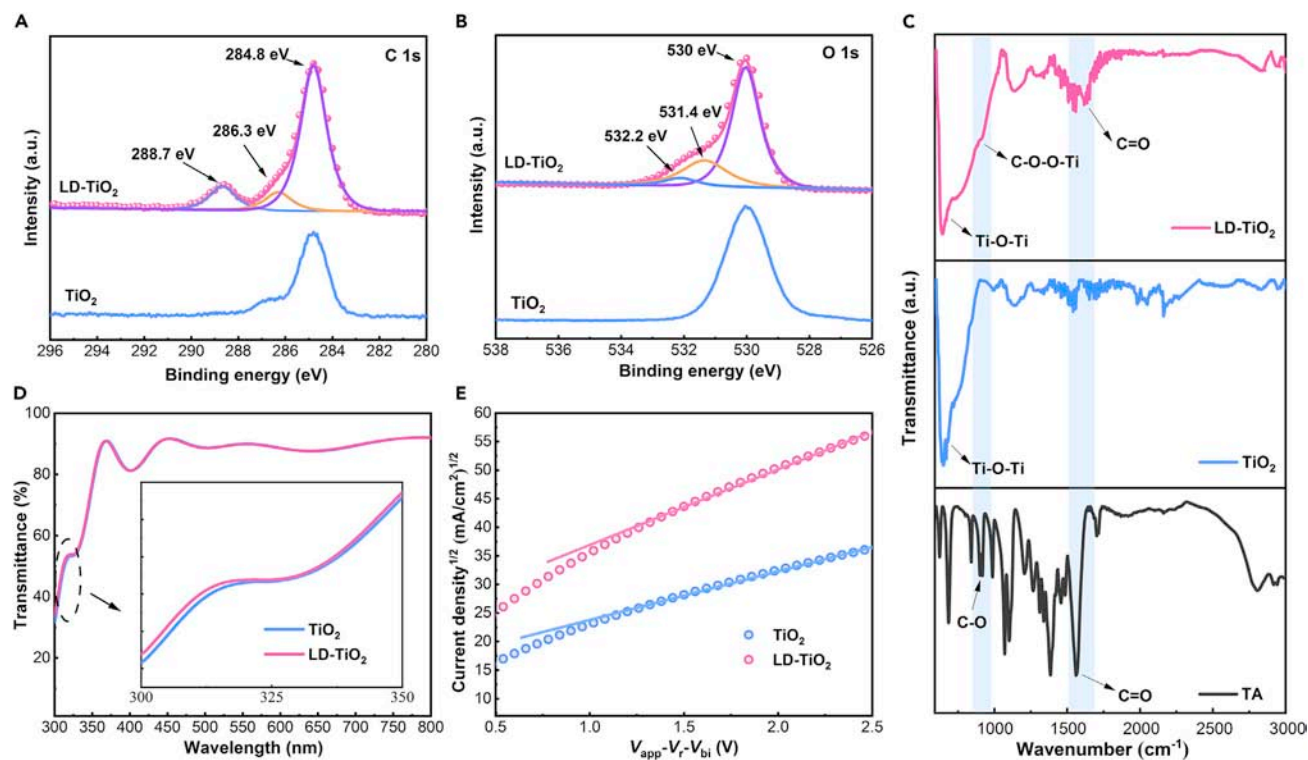
Figure 2. Characterization of TiO₂ film and LD-TiO₂ film
(A and B) C 1s and O 1s spectra of TiO₂ film and LD-TiO₂ film, respectively.
(C) FTIR spectra of TA, TiO₂ film, and LD-TiO₂ film.
(D) Optical transmittance spectra of TiO₂ film and LD-TiO₂ film.
(E) Electron mobility measurements of TiO₂ film and LD-TiO₂ film using the SCLC model.

and the intensity enhancement of O–H peak in comparison with O 1s peak of TiO₂, which also confirms the existence of TA. Meanwhile, as shown in Figure S4B, both the Ti 2p$_{3/2}$ peak and Ti 2p$_{1/2}$ peak shift 0.1 eV of LD-TiO₂ compared with the Ti 2p of TiO₂, which suggests the TA chemical bonded with Ti atom. Fourier transform infrared spectrometer (FTIR) was also performed to explore the existence of TA and its interaction with TiO₂ (Figure 2C). The broad peak at 600–700 cm^{-1} that is shared by TiO₂ and LD-TiO₂ represents the stretching vibration of the Ti–O–Ti group.[30,31] The peak at 1,560 cm^{-1} corresponds to the C=O group stretching vibration of TA.[32] After complexing with TiO₂, the peak shift to 1,618 cm^{-1} in LD-TiO₂, which not only confirms the existence of TA but also indicates its chemical interaction with TiO₂. For the LD-TiO₂, the slight emerging peak at 910 cm^{-1} is supposed to be ascribed to C–O–O–Ti group,[24] further indicating the existed chemical interaction in LD-TiO₂.

As ETL in planar PSCs, the optical and electronic properties of TiO₂ should also be considered carefully. As shown in Figure 2D, both films exhibit a high transmittance in the range of 300–800 nm, which facilitates a high current density of planar PSCs. In detail, in the range of 300–400 nm, the transmittance is slightly increased with the LD strategy. In addition, the conductivity of both films was tested (Figure S5): the conductivity of LD-TiO₂ is obviously larger than that of TiO₂. In order to quantify the electron mobility of the TiO₂ and LD-TiO₂ films, the space charge-limited current (SCLC)[33] method was employed (Figure 2E). The electron mobility of LD-TiO₂ is 4.51 × 10^{-5} cm² V^{-1} s^{-1}, which is almost twice as large as that
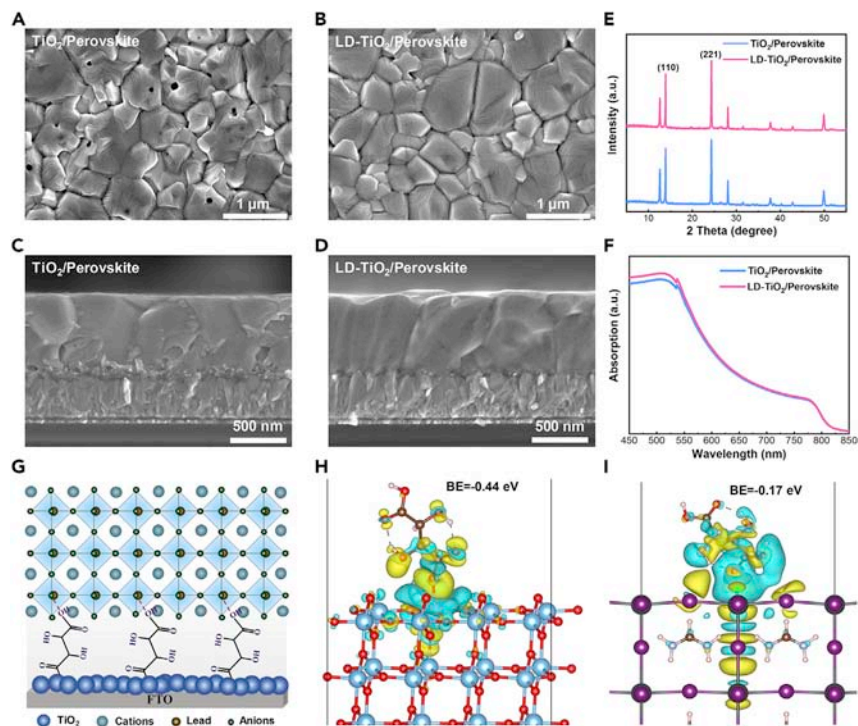
Figure 3. Characterization of perovskite films and cross-linked structure
(A and B) Top-view SEM images of perovskite films deposited on TiO_2 film and LD-TiO_2 film.
(C and D) Cross-sectional SEM images of perovskite films deposited on TiO_2 film and LD-TiO_2 film.
(E) XRD patterns of perovskite films deposited on TiO_2 film and LD-TiO_2 film.
(F) UV-vis absorption spectra of perovskite films deposited on TiO_2 film and LD-TiO_2 film.
(G) Schematic illustration of cross-linked structure at the LD-TiO_2/perovskite interface.
(H) Side-view of the relaxed model for TA connected on the (101) oriented TiO_2 surface.
(I) Side-view of the relaxed model for TA connected on the (001) oriented $FAPbI_3$ buried surface.

(1.82×10^{-5} cm^2 V^{-1} s^{-1}) of TiO_2. The enhanced electron mobility may result from the vacant orbitals of the Ti atom filled by lone-pair electrons of ligands and inhibited crystal particle aggregation.

Optimized perovskite film and cross-linked structure
The surface topography of TiO_2 that is applied as ETL in planar PSCs has a significant effect on the crystalline quality of perovskite film, including grain size, microstructure, and surface coverage. We used a two-step spin-coating method to fabricate perovskite film on TiO_2 and LD-TiO_2, and then carried out SEM, X-ray diffraction (XRD) and UV-vis absorption to observe the film properties. In Figure 3A, we can obviously catch the sight of pinholes universally distributed over the whole perovskite film. The pinholes may result from the agglomerations on the TiO_2 surface, which leads to inhomogeneous crystal growth. In comparison, the perovskite film on LD-TiO_2 (Figure 3B) is compact and pinhole free, and the average grain size is slightly larger than that of perovskite film on TiO_2 (Figure S6). From the cross-sectional images of perovskite films (Figures 3C and 3D), we can also notice that the perovskite film on LD-TiO_2 is dense with the grains penetrating the substrate, which is conducive to efficient carrier transport. The AFM was also carried out to observe the perovskite films on different substrates (Figure S7; Note S1), which is in consistence with the SEM results. In addition, the Kelvin probe force microscopy (KPFM) results (Figure S8; Note S2) suggest that the LD deposition strategy

has a negligible influence on Fermi level of the perovskite. Based on the thin-film nucleation and growth mechanism, in the process of heterogeneous nucleus formation, the Gibbs free energy (ΔG) is closely related to the microstructure of the substrate. The ΔG can be calculated from the following equation:

$$\Delta G_{heterogeneous} = \Delta G_{homogeneous} \times f(\theta) \text{ with } f(\theta) = \frac{(2 - 3\cos\theta + \cos^3\theta)}{4}$$

In the equation, the θ is the contact angle of the precursor on the substrate. Since the value of θ is between 0 and $\pi/2$, the larger the θ is, the larger the $f(\theta)$ is, which suggests that a smaller contact leads to a decreased ΔG. Compared with TiO_2, the LD-TiO_2 exhibits a smoother surface with smaller roughness, which conduces to a smaller contact angle of precursor on the substrate, promoting the nucleation process of perovskite film. Therefore, the inhibited TiO_2 aggregation is conducive to reduce contact angle, assisting the perovskite uniform nucleation.

The XRD patterns of perovskite films on different substrates are shown in Figure 3E, and both the perovskite films share similar peaks that correspond to the typical diffraction peaks of perovskite reported in the previous articles.[34] We carefully calculated the full width at half maxima (FWHM) of (110) and (221) peaks of perovskite film on both substrates (Figure S9). The decreased FWHM of perovskite film on LD-TiO_2 indicates the improved perovskite crystallinity. The optical property of perovskite films was also researched using UV-vis absorption measurement (Figure 3F). Compared with the perovskite film on TiO_2, the perovskite film on LD-TiO_2 exhibits a slightly higher absorption, especially in the range of 450–550 nm, which helps to obtain a higher current density of LD-TiO_2-based planer PSCs.

The ETL/perovskite interfacial structure has a significant impact on the electron extraction, which needs to be carefully researched. From the cross-sectional images shown in Figures 3C and 3D, we can distinctly observe the microstructure of the ETL/perovskite interface. Compared with the rugged and jagged TiO_2/perovskite interface that is impacted by the surface topography of TiO_2, the LD-TiO_2/perovskite interface is compact and continuous, which helps to reduce interfacial bulk defects and contact impedance. In addition, as shown in Figure 3G, the TA molecular can passivate the surface oxygen vacancy through connecting with Ti atom, and cross-link with perovskite film through connecting with Pb atom by –COOH group. We carried out density functional theory (DFT) calculation to investigate the interconnection property of cross-linked TA molecular. After structure optimization, we calculated the binding energy (BE) of TA on the TiO_2 surface (Figure 3H) according to the equation of BE = $E_{surface+TA} - E_{surface} - E_{TA}$, where $E_{surface+TA}$, $E_{surface}$, and E_{TA} were the total free energy of TA-connected TiO_2 surface, TiO_2 surface, and one TA molecule, respectively. The calculated BE between TiO_2 and TA is -0.44 eV, indicating the strong interconnection between TiO_2 and TA molecular. At the LD-TiO_2/perovskite interface, the BE between TA and perovskite film was also calculated (Figure 3I). In our work, the perovskite is $FA_{0.92}MA_{0.08}PbI_3$, according to the previous reports.[25] During the DFT calculation, the perovskite model was decided as $FAPbI_3$. The calculated BE is -0.17 eV, which demonstrates the feasible connection of TA with Pb atom, and helps to reduce unsaturated Pb^{2+} defects. The TA molecular linked with both TiO_2 and perovskite can enhance the interfacial contact and reduce interfacial defects, which is conducive to efficient electron extraction and suppressed non-radiative recombination.

Improved performance of planar PSCs

After researching the influence of LD strategy on TiO_2 and perovskite film, we fabricated planar PSCs structured as FTO/TiO_2 (LD-TiO_2)/$FA_{0.92}MA_{0.08}PbI_3$/Spiro-OMeTAD/Au
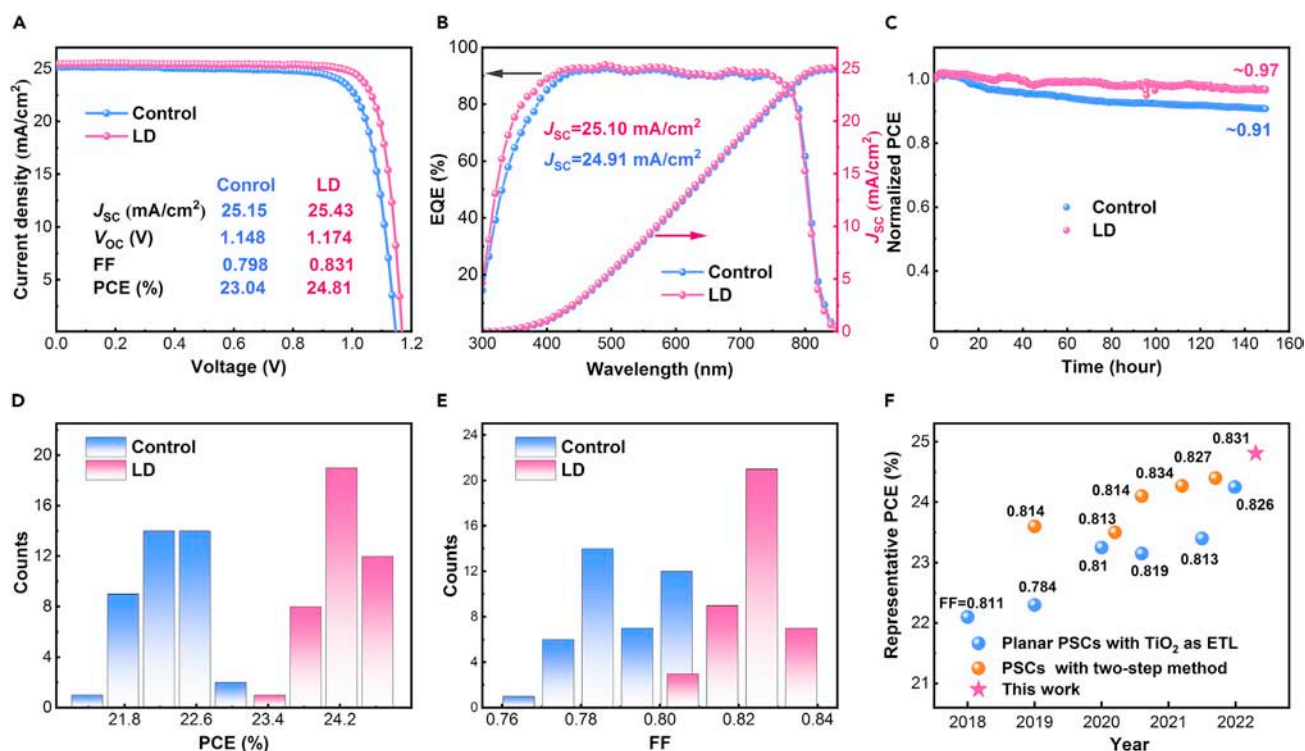
Figure 4. Performance of the planar PSCs with various ETLs

(A) J-V curves (reverse scan) of the champion planar PSCs with various ETLs, the area of the cell is 0.08053 cm^2.

(B) The corresponding EQE and integrated current density curves of planar PSCs with various ETLs.

(C) Operational stability tracking of cells under steady-state light illumination and bias voltage for 150 h (Ar atmosphere, white LED, and uncontrollable temperature).

(D) Statistical results of PCEs (reverse scan) fitted from 40 planar PSCs with various ETLs.

(E) Statistical results of FFs (reverse scan) fitted from 40 planar PSCs with various ETLs.

(F) Cross-comparison of PCE between planar PSCs with TiO$_2$ as ETL, PSCs fabricated with a two-step method and PSCs in this work, and the corresponding FF is labeled.

and characterized its performance. We first explored the influence of introduced TA concentration on the PCE. As shown in Figure S10 and Table S1, the PCE of planar PSCs shows an increasement with the LD strategy, especially reflecting in the increasement of fill factor (FF). In detail, the highest PCE of 24.3% is obtained at the optimal concentration of 0.3 mmol (the molar ratio of TA/TiCl$_4$ is 1.05%). With the amount increasing to 0.4 mmol, the PCE slightly decreases from 24.3% to 24.0%, and the FF decreases from 0.82 to 0.814, which may result from the excess TA molecular impacting the electronic of TiO$_2$. Hereafter, the data of planar PSCs with LD-TiO$_2$ are collected with the amount of TA being 0.3 mmol.

The planar PSCs with LD-TiO$_2$ exhibits a champion PCE (Figure 4A) of 24.81%, which is significantly superior to that (23.04%) of the control PSCs. Among the photovoltaic parameters, the FF of PSCs with LD-TiO$_2$ also exhibits a drastically improvement from 0.798 to 0.831. Encouragingly, the certificated PCE of planar PSCs with LD-TiO$_2$ is 24.5% (Figure S11), the highest certificated PCE of planar PSCs with TiO$_2$ as ETL reported to date. We also investigated the hysteresis of planar PSCs with different ETLs. As shown in Figure S12 and Table S2, the hysteresis factor of PSCs with LD-TiO$_2$ is 2.46%, which is smaller than that (3.52%) of control PSCs. The corresponding external quantum efficiency (EQE) of PSCs with LD-TiO$_2$ is slightly higher

than that of control PSCs, especially in the range of 300–400 nm (Figure 4B), which agrees with the transmittance results of TiO_2 and LD-TiO_2 mentioned above. The integrated J_{SC} of PSCs with LD-TiO_2 is 25.10 mA/cm^2, indicating a good matching with the measured J_{SC} shown in Figure 4A. The operational stability of PSCs with TiO_2 and LD-TiO_2 was measured (Figures 4C and S13; Note S3). The PSCs with LD-TiO_2 show a stable power output and maintain 97% of their initial state after 150 h under continuous light soaking.

We gathered photovoltaic parameters of 40 planar PSCs with TiO_2 and LD-TiO_2, respectively, to explore the reproducibility of PSCs. The PCE and FF distribution histograms are shown in Figures 4D and 4E, with the corresponding statistics listed in Tables S3 and S4. As expected, the PSCs with LD-TiO_2 exhibit outstanding reproducibility, which is better than that of control PSCs. The improved repeatability results from the controlled deposition of ETL. Detailly, the average PCE of PSCs with LD-TiO_2 is 24.22%, and all the FFs of PSCs with LD-TiO_2 are up to 0.8, indicating the excellent electron transport within the devices. Finally, based on the planar PSCs with TiO_2 as ETL, we made a comparison between the previous reports and this work (Figure 4F; Table S5). Over the last 5 years, although the PCE of TiO_2-based planar PSCs has always been rising, it is still far from 25%. Compared with the reported works, we obtained a PCE of 24.81%, which significantly promotes the advance of TiO_2-based planar PSCs. In addition, we also made a list of reported representative PCE of PSCs that are fabricated with a two-step method (Figure 4F; Table S6). It is noted that the PCE obtained in this work is also one of the highest PCE among the reported works whose PSCs are fabricated with a two-step method, which further demonstrates the positive effects of our strategy on the performance of PSCs.

Origin of the improved performance and device physics

To gain an insight into the electron transport dynamic, various measurements were performed on PSCs with TiO_2 and LD-TiO_2. The electrochemical impedance spectroscopy (EIS) measurement was carried out to explore the interfacial electron transport and recombination (Note S7). The PSCs were tested in ambient air under dark conditions, and the spectra were obtained in the range of 0.1 Hz to 100 kHz. From Figure 5A, we can notice a completed semicircle and an unfinished semicircle. It is reported that the semicircle located in the high-frequency region is responding to impedance (R_{ct}) arising from the charge transport between the electron (hole) transport layer with the perovskite layer, and the semicircle located in the low-frequency region is associated with the carrier recombination impedance (R_{re}).[35] After fitting the curves (Table S7), the R_{ct} of PSCs with LD-TiO_2 is obviously lower than that of control PSCs, indicating a better ETL/perovskite interfacial contact. In addition, to further explore the influence of LD on ETL/perovskite interfacial contact impedance directly, we tested the impedance of PSCs with TiO_2 and LD-TiO_2 at different frequencies (Figure S14). It is found that the impedance of PSCs with LD-TiO_2 is obviously lower than that of the control device. To eliminate the influence of perovskite/Spiro-OMeTAD interface on the impedance, the devices structured as FTO/TiO_2 (LD-TiO_2)/$FA_{0.92}MA_{0.08}PbI_3$/Au were also measured (Figure S15). The result is in consistence with Figure S14, suggesting the LD strategy can significantly decrease the ETL/perovskite interfacial contact impedance. To confirm that the reduced interfacial contact impedance improves the FF of planar PSCs, we explored the photovoltaic parameters verse interfacial impedance evolution using the wxAMPS program, which has been broadly used to simulate thin-film solar cells.[1,36] During the simulation, the impedance evolution is controlled by regulating the interfacial carrier mobility. For simulation accuracy, we split the ETL into two parts: one is the ETL
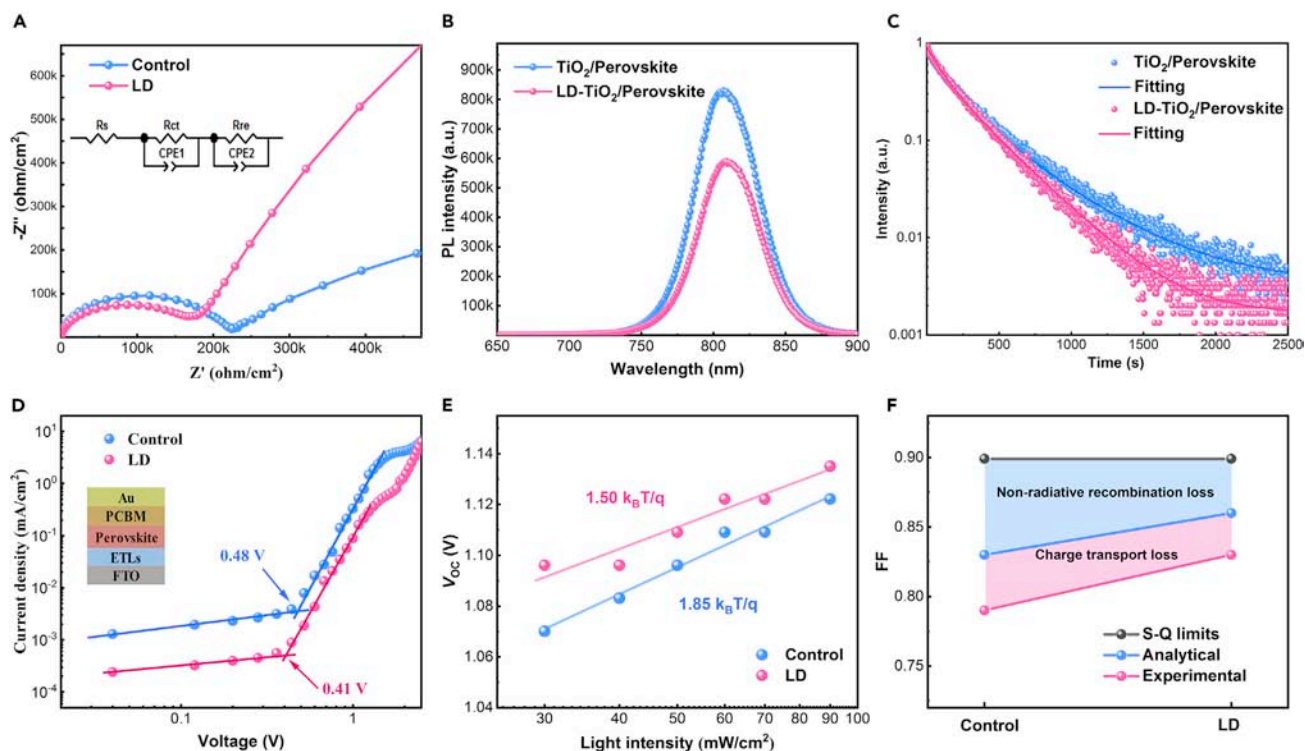
Figure 5. Characterization of interfacial charge transport and device physical property
(A) EIS spectra of planar PSCs with various ETLs.
(B) Steady-state PL spectra of perovskite films deposited on TiO_2 film and LD-TiO_2 film.
(C) TRPL spectra of perovskite films on the TiO_2 film and LD-TiO_2 film.
(D) Dark J-V curves of electron-only devices with various ETLs.
(E) V_{OC} of PSCs with various ETLs plotted against the logarithm of light intensity.
(F) Plots of the SQ-limit FF, analytical FF, and the experimental FF for PSCs with various ETLs. The FF limitation can be split into non-radiative recombination losses (blue area) and charge transport losses (pink area).

that is 45 nm, and another is the interfacial ETL that is 5 nm named L2 (Figure S16). The operation on the perovskite layer is the same as that of ETL, and the interfacial perovskite layer is named L1. The corresponding parameters used in this simulation are shown in Table S8. It is clear to find that the increased ETL/perovskite interfacial contact impedance (reduced interfacial carrier mobility) impacts the FF badly (Figure S17A), meanwhile, its impact on J_{SC} and V_{OC} is negligible (Figure S17B). Thus, the FF improvement of planar PSCs with the LD strategy may result from the reduced ETL/perovskite interfacial contact impedance.

The ETL/perovskite interfacial electron transport was further to be researched by steady-state photoluminescence (PL) and time-resolved PL (TRPL). The PL spectrum (Figure 5B) of perovskite film on LD-TiO_2 exhibit an obvious intensity quenching compared with that of perovskite film on TiO_2. It is noticed that the TRPL decay spectra (Figure 5C; Table S9; Note S8) are composed of a fast decay component and a slow decay component. The τ_1 of LD-TiO_2/perovskite is 105.14 ns, obviously smaller than that of TiO_2/perovskite (188.41 ns). The τ_{ave} decreases from 320.36 to 262.63 ns with LD strategy. These results indicate the efficient electrons extraction with the reduced nonradiative loss.[35,37] The improved capability for electron extraction of LD-TiO_2 may have two reasons: one reason is that the LD strategy improves the electron mobility of TiO_2, promoting the electron transport effectively; another is that

the ETL/perovskite interface contact property has been optimized due to cross-linked structure and smoother LD-TiO$_2$ film.

We prepared electron-only devices and measured their dark *J-V* curves (Figure 5D) to quantitively estimate the defect density of the perovskite layer according to the equation of N$_t$ = eL^2/2εε$_0$V$_{TFL}$, where ε is the relative dielectric constant, ε$_0$ the vacuum permittivity, e the electron charge, L the thickness of perovskite film and V$_{TFL}$ the trap-filled limit voltage. The V$_{TFL}$ of PSCs with LD-TiO$_2$ is 0.41 V, and the calculated N$_t$ is 3.43 × 10^{15}/cm^3, which is smaller than that (4.02 × 10^{15}/cm^3) of control PSCs. Due to both the PSCs sharing the same hole transport layer (HTL), the reduced defect density is supposed to result from the ETL/interfacial defects passivation and the improved crystallinity of perovskite film. In addition, the ideality factor (n_{ID}) was measured to further explore the influence of LD strategy on planar PSCs. We gathered the V_{OC} of both PSCs verse light intensity to calculate the n_{ID} according to the following equation:

$$V_{OC} = \frac{n_{ID} k_B T}{q} \ln(I)$$

Where k_B is the Boltzmann constant, T the thermodynamic temperature, and q the electron charge. The n_{ID} of PSCs with LD-TiO$_2$ is 1.50 (Figure 5E), which is smaller than that (1.85) of control PSCs, indicating the reduced non-radiative carrier recombination within PSCs with LD-TiO$_2$. To explain the improvement of FF, we carefully considered the non-radiative carrier recombination losses and charge transport losses that are the reasons for reducing the FF value below the S-Q limit.[38,39] As shown in Figure 5F, the analytical maximum FF can be calculated according to the following equation:

$$FF_{max} = \frac{\nu_{oc} - \ln(\nu_{oc} + 0.72)}{\nu_{oc} + 1} \quad with \ \nu_{oc} = \frac{qV_{OC}}{n_{ID} k_B T}$$

We calculate the maximum FF of both PSCs in case there is no transport loss, and then we add the S-Q FF value and the experimental FF value to make a direct comparison. We can find that both the non-radiative recombination losses and charge transport losses in PSCs with LD-TiO$_2$ are smaller than that in control PSCs, resulting from the decreased ETL/perovskite interfacial contact impedance and carrier recombination.

Improved stability of planar PSCs

The stability issue of TiO$_2$-based planar PSCs under UV irradiation has attracted huge attention. Before explored the influence of LD strategy on UV stability of PSCs, we monitored the PCE evolution of unencapsulated PSCs with TiO$_2$ and LD-TiO$_2$ upon exposure to ambient air (25°C and ∼10% relative humidity) under dark conditions for 2,000 h. The PCE of PSCs with LD-TiO$_2$ can maintain ∼95% of its initial highest value after aging (Figure 6A). In comparison, the PCE of PSCs with TiO$_2$ can only maintain ∼80%. The enhanced humidity stability can be ascribed to the optimized ETL/perovskite interface and optimized perovskite film. To explore the influence of LD strategy on UV stability of planar PSCs, we utilized a harsh experiment using the Philip UV lamp (λ = 254 nm) to continuously irradiate the PSCs with TiO$_2$ and LD-TiO$_2$ at room temperature in a glove box filled N$_2$. The intensity of the UV lamp applied in our experiment is 50 mW/cm^2. Figure S18 shows the experiment situation: the actual temperature of the tested devices was ∼50°C measured with the thermo-detector.

As for the control PSCs, the PCE curve shows a two-stage decay phenomenon (Figure 6B): in the first stage, the decay rate is relatively slow, and in the second stage, the decay rate is higher. Such a two-stage UV degradation of TiO$_2$-based PSCs is highly consistent with the reported article published in 2020.[10] After 1,200 h of UV radiation, the PSCs with LD-TiO$_2$ can maintain ∼87% of their initial PCE, while the control PSCs
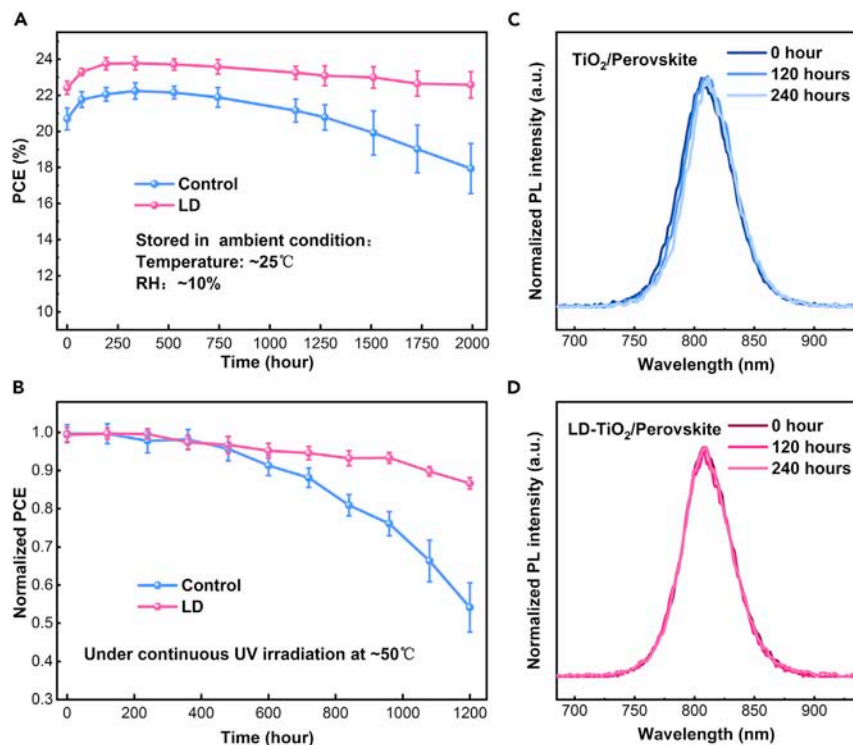
Figure 6. Stability of the planar PSCs with various ETLs

(A) The PCE evolution of unencapsulated 10 individuals.

(B) The evolution of PCE. The unencapsulated 10 PSCs with TiO_2 and LD-TiO_2 are under continuous 254-nm UV irradiation with an intensity of 50 mW/cm^2 at glove box filled N_2.

(C and D) Normalized PL spectra of perovskite films deposited on TiO_2 film and LD-TiO_2 film. The samples structured as FTO/TiO_2 (LD-TiO_2)/perovskite are under continuous 254 nm UV irradiation with an intensity of 50 mW/cm^2, and the UV light incident direction is from FTO side.

can only maintain ~54%, indicating a significantly enhanced UV stability resulting from the LD strategy. The FF decay curve was also considered (Figure S19), and the PSCs with LD-TiO_2 can maintain ~93% of their initial FF, which further confirms that the ETL/perovskite interface is significantly optimized by the LD strategy as analyzed above. Under UV irradiation, the perovskite film deposited on TiO_2 can be decomposition due to the photocatalytic property of TiO_2. UV-vis absorption and PL measurements were carried out to research the stability of perovskite films on TiO_2 and LD-TiO_2. As shown in Figures 6C and 6D, the PL spectrum of perovskite film on TiO_2 shifts slightly under UV irradiation for 240 h, indicating the decomposition of the perovskite film.[40] Encouragingly, we found that the perovskite film on LD-TiO_2 exhibits no shift trend. The absorption spectra of perovskite films on TiO_2 and LD-TiO_2 under UV irradiation are shown in Figures S20A and S20B. Although both the perovskite films display the absorption intensity decay under continuous UV irradiation from the FTO side for 1,008 h, the perovskite on LD-TiO_2 shows better stability, which is in agreement with the PL measurement. Both the PCE decay curves and optical spectra measurements confirm that the LD strategy can effectively suppress the adverse effect of TiO_2 on perovskite film and planar PSCs under UV irradiation, which mainly results from the passivated Ti^{3+}-V_O (oxygen vacancy) defects due to the ligand coordination bonding with Ti atom (Note S4; Figures S21 and S22).

Extension of the LD strategy

The LD strategy based on the coordination ability of ligands was further to be confirmed by EDTA. We introduced the EDTA (the chemical structure shown in

Figure S23) as a ligand to chemical bath precursor and fabricated TiO_2 film (EDTA-TiO_2). First, we utilized AFM to characterize the surface topography of EDTA-TiO_2 (Figure S24A) and quantified its RMS as 17.7 nm, which is smaller than that (42 nm) of TiO_2. After confirming the existence of EDTA (Figure S24B), which can distribute in the bulk of LD-TiO_2 (Figure S25; Note S5) and improved electron mobility of EDTA-TiO_2 (Figure S24C), we collected the photovoltaic parameters of PSCs with EDTA-TiO_2 (Figure S24D): the PSCs with EDTA-TiO_2 possess a champion PCE of 24.5% and an average PCE of 24.1%. In addition, the enhanced UV stability of PSCs with EDTA-TiO_2 was also proved by the PCE decay curve and absorption spectra evolution (Figures S24E and S24F), indicating the subtle adverse impact of EDTA-TiO_2 on perovskite film under continuous UV irradiation.

Except from considering TA and EDTA as the introduced ligands that including multiple –COOH groups, we further explore the possibility of PA, pyrocatechol (PY) and N-cyclohexyltaurine (NC) as the ligands, respectively (Figures S26 and S27; Tables S10 and S11; Note S6). Although the PSCs with PY-TiO_2 exhibited a bad repeatability, the champion PCE and average PCE of PSCs have been effectively improved after regulation with LD strategy using all these ligands compared with control device, indicating that the LD strategy exhibits an excellent reliability and broad applicability. Properly speaking, for choosing the ligands to obtain an ideal effect, it is suggested to comprehensively consider the coordination ability and the molecular steric configuration and size. Furthermore, properties (such as color and alkalinity) of the target materials are advised to be cautioned.

Conclusions

In summary, the LD strategy has been proposed to precisely regulate TiO_2 film and interfacial structure based on the coordination ability of ligands. Owing to inhibited particle aggregation, decreased ETL/perovskite interfacial contact impedance and enhanced electron extraction, the planar PSCs with LD-TiO_2 obtain a PCE of 24.81% (certificated 24.5%), the highest value among TiO_2-based planar PSCs reported so far. It is also noted that the obtained PCE breaks the record of reported PSCs with a two-step fabricating method to date. In addition, both the UV and humidity stability of TiO_2-based planar PSCs have been distinctly enhanced. We believe that the proposed LD strategy can also be well applied in the deposition of other inorganic ETL such as SnO_2 and ZnO, providing more opportunities to push forward the development of planar PSCs and other optoelectronic devices.

EXPERIMENTAL PROCEDURES

Resource availability

Lead contact

Further information and requests for resources should be directed to and will be fulfilled by the lead contact, Meicheng Li (mcli@ncepu.edu.cn).

Materials availability

This study did not generate new unique materials.

Data and code availability

This study did not generate any datasets.

Materials

All the materials used in this work were utilized as received without any further purification. For the materials used for ETL fabrication: $TiCl_4$ (purity: 99.9%)

precursor was purchased from Alfa Aesar, DL-TA was purchased from Innochem. For the materials used for perovskite fabrication: methylammonium iodide (MAI), formamidinium iodide (FAI), and methylammonium chloride (MACl) were purchased from Xi'an Polymer Light Technology, lead iodide (purity: 99.999%) was purchased from Alfa Aesar, N,N-dimethylformamide (DMF), dimethyl sulfoxide (DMSO), and isopropanol were purchased from Acros Organics (extra dry). For the materials used for HTL fabrication: 2,2',7,7'-tetrakis (N,N-di-p-methoxyphenylamine)-9,9'spirobifluorene (Spiro-OMeTAD), bis(trifluoromethane) sulfonimide lithium salt (Li-TFSI), and 4-tert-butylpyridine (tBP) were purchased from Xi'an Polymer Light Technology. Acetonitrile (ACN) was purchased from Sigma-Aldrich.

Fabrication

Solution preparation

TiO_2 solution was prepared according to the report of Wei et al.[11] 3 mL of $TiCl_4$ precursor was put into 150 mL deionized water, then stir it up. LD-TiO_2 solution was prepared with 3 mL of $TiCl_4$ precursor was put into 150 mL deionized water with 45 mg TA, then stir it up. To prepare PbI_2 precursor solution: 690.5 mg PbI_2 was put into 1 mL DMF and DMSO mixture with the volume ratio is 9:1. To prepare organic ammonium salt solution, 90 mg FAI, 6.4 mg MAI, and 9 mg MACl were put into 1 mL IPA. To prepare phenylethylamine iodine (PEAI) precursor solution, 5 mg PEAI was put into 1 mL IPA. To prepare Spiro-OMeTAD solution: 80 mg Spiro-OMeTAD, tBP 30 μL and 20 μL Li-TFSI (520 mg/mL in ACN) put into 1 mL chlorobenzene.

Solar cell fabrication

FTO glass (7 $\Omega \cdot sq^{-1}$) was ultrasonic cleaned sequentially with deionized water, ethyl alcohol, and deionized water for 20 min, respectively. After UV-ozone, TiO_2 (LD-TiO_2) films were fabricated by chemical bath deposition for 40 min at 70°C. Then, the TiO_2 (LD-TiO_2) films were further treated by nitrogen purging and drying oven storing before next step in the glove box. To fabricate perovskite film, the PbI_2 solution was spin-coated on TiO_2 (LD-TiO_2) film at 1,500 rpm for 30 s, then annealed at 70°C for 1 min, after cooling down, the organic ammonium salt solution was spin-coated on PbI_2 film at 2,000 rpm for 30 s, then annealed at 150°C for 10 min under ambient air conditions (40%–50% relative humidity). The PEAI solution was spin-coated on fabricated perovskite film at 5,000 rpm for 30 s, followed by thermal annealing at 100°C for 1 min. On the surface of PEAI, Spiro-OMeTAD film was deposited by spin-coating at 4,000 rpm for 30 s. At last, Au electrode was thermal-evaporated on the top.

Characterization

To analyze the topography of TiO_2 (LD-TiO_2) and perovskite films, the Hitachi SU8010 field-emission SEM and FMNanoview 1,000 AFM were carried out. To characterize the TiO_2 (LD-TiO_2), XPS spectra were measured by Thermo Fisher Scientific ESCALAB 250Xi, FTIR spectra were measured by Bruker INVENIO, and the transmittance spectra were measured by UV-vis spectrophotometer (UV-2600), which was also carried out for absorption tests of perovskite films. The XRD patterns of perovskite films were collected using Bruker D8 Advance X-ray diffractometer. The J-V performance of PSCs was measured via a source meter (Keithley 2400) along with AM 1.5G irradiation with a power density of 100 mW·cm^{-2}, and the light intensity was calibrated by a National Institute of Metrology-certified standard Si solar cell. The J-V curves of PSCs were obtained at forward (from −0.1 to 1.2 V) or reverse (from 1.2 to −0.1 V) scan direction with the scanning speed of 0.06 V/s. The EQE spectra were measured via QE-R systems (Enli Tech.). To gain an insight

into the charge transport dynamic of PSCs, the EIS data were obtained via an electrochemical workstation (Zahner Zennium). Impedance spectra were measured using HIOKI impedance analyzer (IM 3570). PL and TRPL spectra of perovskite films were measured via FLS 980 (Edinburgh Instruments), and the wavelength of excitation light is 470 nm.

DFT calculation

The models of TA on TiO_2 and $FAPbI_3$ were investigated by the Vienna *ab initio* simulation package (VASP) using the Perdew-Burke-Ernzerh (PBE) functional of the generalized gradient approximation (GGA).[41–44] Here, the valence electron configurations of the atoms are described as follows: H $(1s^1)$, C $(2s^22p^2)$, N $(2s^22p^3)$, O $(2s^22p^4)$, Ti $(3d^34s^1)$, I $(5s^25p^5)$, and Pb $(6s^26p^2)$. The surfaces of TiO_2 and $FAPbI_3$ were simulated by their typical (101) and (001) surfaces, respectively. The 3×2 and 2×2 supercell models with 3 units layers were used to describe the models of (101)-TiO_2 and (001)-$FAPbI_3$ surfaces. A vacuum of about 40 Å was added between two slabs to eliminate the interactions between repeated slabs. The TA was located on the surface of each slab. The plane-wave cutoff energy was set to 520 eV. Considering the size of supercells, the geometry optimization calculations were only performed at the gamma point. After geometry optimization calculations, the convergence criterion for ionic relaxations was set to 10^{-5} eV between two consecutive steps. The Monkhorst-Pack k-point mesh of $2 \times 2 \times 1$ were adopted to calculate the relative properties of TA with TiO_2 (or $FAPbI_3$). The BE of TA on TiO_2 (or $FAPbI_3$) was calculated by the following formula: BE $= E_{surface+TA} - E_{surface} - E_{TA}$, where $E_{surface+TA}$, $E_{surface}$, and E_{TA} were the total free energy of TA-connected TiO_2 (or $FAPbI_3$) surface, TiO_2 (or $FAPbI_3$) surface, and one TA molecule, respectively.

SUPPLEMENTAL INFORMATION

Supplemental information can be found online at https://doi.org/10.1016/j.joule.2022.07.004.

AUTHOR CONTRIBUTIONS

H.H. and M.L. conceived the idea. M.L. guided the work as supervisor. H.H. and P.C. did experimental designs, device fabrication, and data analysis. L.Y., X.Y., Q.Z., S.Q., and S.D. participated in the device fabrications and some material and device characterizations. Y.C., Xin Wang, and X.D. did DFT calculation and data analysis. Xinxin Wang, B.L., Z.L., and Y.Y. supported the measurement system construction, device fabrication, characterization, and discussions. H.H., P.C., and M.L. participated in manuscript writing and revising. J.J., X.Z., Y.L., and M.L. polished the manuscript language. All authors were involved in the discussions and approved the manuscript.

Joule
Article

DECLARATION OF INTERESTS

The authors declare no competing interests.

REFERENCES

1. Cui, P., Wei, D., Ji, J., Huang, H., Jia, E., Dou, S., Wang, T., Wang, W., and Li, M. (2019). Planar p–n homojunction perovskite solar cells with efficiency exceeding 21.3. Nat. Energy *4*, 150–159.

2. Xiao, K., Lin, R., Han, Q., Hou, Y., Qin, Z., Nguyen, H.T., Wen, J., Wei, M., Yeddu, V., Saidaminov, M.I., et al. (2020). All-perovskite tandem solar cells with 24.2% certified efficiency and area over 1 cm² using surface-anchoring zwitterionic antioxidant. Nat. Energy *5*, 870–880.

3. Xiao, K., Wen, J., Han, Q., Lin, R., Gao, Y., Gu, S., Zang, Y., Nie, Y., Zhu, J., Xu, J., and Tan, H. (2020). Solution-processed monolithic all-perovskite triple-junction solar cells with efficiency exceeding 20. ACS Energy Lett *5*, 2819–2826.

4. Huang, H., Yan, H., Duan, M., Ji, J., Liu, X., Jiang, H., Liu, B., Sajid, S., Cui, P., Li, Y., and Li, M. (2021). TiO₂ surface oxygen vacancy passivation towards mitigated interfacial lattice distortion and efficient perovskite solar cell. Appl. Surf. Sci. *544*, 148583.

5. Jiang, Q., Zhang, L., Wang, H., Yang, X., Meng, J., Liu, H., Yin, Z., Wu, J., Zhang, X., and You, J. (2017). Enhanced electron extraction using SnO₂ for high-efficiency planar-structure HC(NH₂)₂PbI₃-based perovskite solar cells. Nat. Energy *2*, 16177.

6. Wang, Z., Zhu, X., Feng, J., Wang, C., Zhang, C., Ren, X., Priya, S., Liu, S.F., and Yang, D. (2021). Antisolvent- and annealing-free deposition for highly stable efficient perovskite solar cells via modified ZnO. Adv. Sci. *13*, 2006860.

7. Min, H., Lee, D.Y., Kim, J., Kim, G., Lee, K.S., Kim, J., Paik, M.J., Kim, Y.K., Kim, K.S., Kim, M.G., et al. (2021). Perovskite solar cells with atomically coherent interlayers on SnO₂ electrodes. Nature *598*, 444–450.

8. Yoo, J.J., Seo, G., Chua, M.R., Park, T.G., Lu, Y., Rotermund, F., Kim, Y.K., Moon, C.S., Jeon, N.J., Correa-Baena, J.P., et al. (2021). Efficient perovskite solar cells via improved carrier management. Nature *590*, 587–593.

9. Li, Y., Chen, Z., Yu, B., Tan, S., Cui, Y., Wu, H., Luo, Y., Shi, J., Li, D., and Meng, Q. (2022). Efficient, stable formamidinium-cesium perovskite solar cells and minimodules enabled by crystallization regulation. Joule *6*, 676–689.

10. Ji, J., Liu, X., Jiang, H., Duan, M., Liu, B., Huang, H., Wei, D., Li, Y., and Li, M. (2020). Two-stage ultraviolet degradation of perovskite solar cells induced by the oxygen vacancy-Ti⁴⁺ states. iScience *4*, 101013.

11. Wei, D., Ji, J., Song, D.D., Li, M., Cui, P., Li, Y., Mbengue, J.M., Zhou, W.J., Ning, Z.J., and Park, N.-G. (2017). A TiO₂ embedded structure for perovskite solar cells with anomalous grain growth and effective electron extraction. J. Mater. Chem. A *5*, 1406–1414.

12. Hu, W., Wen, Z., Yu, X., Qian, P., Lian, W., Li, X., Shang, Y., Wu, X., Chen, T., Lu, Y., et al. (2021). In situ surface fluorination of TiO₂ nanocrystals reinforces interface binding of perovskite layer for highly efficient solar cells with dramatically enhanced ultraviolet-light stability. Adv. Sci. (Weinh) *8*, 2004662.

13. Paik, M.J., Lee, Y., Yun, H.S., Lee, S.U., Hong, S.T., and Seok, S.I. (2020). TiO₂ colloid-spray coated electron-transporting layers for efficient perovskite solar cells. Adv. Energy Mater. *10*, 2001799.

14. Wu, J., Li, Y., Tan, S., Yu, B., Li, H., Li, Y., Shi, J., Wu, H., Luo, Y., Li, D., and Meng, Q. (2020). Enhanced perovskite solar cell efficiency via the electric-field-induced approach. ACS Appl. Mater. Interfaces *12*, 27258–27267.

15. Tan, H., Jain, A., Voznyy, O., Lan, X., García de Arquer, F.P., Fan, J.Z., Quintero-Bermudez, R., Yuan, M., Zhang, B., Zhao, Y., et al. (2017). Efficient and stable solution-processed planar perovskite solar cells via contact passivation. Science *355*, 722–726.

16. Gao, F., Luo, C., Wang, X., and Zhao, Q. (2021). Alkali metal chloride-doped water-based TiO₂ for efficient and stable planar perovskite photovoltaics exceeding 23% efficiency. Small Methods *5*, e2100856.

17. Zhu, X., Du, M., Feng, J., Wang, H., Xu, Z., Wang, L., Zuo, S., Wang, C., Wang, Z., Zhang, C., et al. (2020). High-efficiency perovskite solar cells with imidazolium-based ionic liquid for surface passivation and charge Transport. Angew. Chem. Int. Ed. Engl. *8*, 4238–4244.

18. Su, H., Zhang, J., Hu, Y., Du, X., Yang, Y., You, J., Gao, L., and Liu, S. (2021). Fluoroethylamine engineering for effective passivation to attain 23.4% efficiency perovskite solar cells with superior stability. Adv. Energy Mater. *11*, 2101454.

19. Nam, H.-D., Lee, B.-H., Kim, S.-J., Jung, C.-H., Lee, J.-H., and Park, S. (1998). Preparation of ultrafine crystalline TiO₂ powders from aqueous TiCl₄ solution by precipitation. Japan. J. Appl. Phys. *37*, 4603–4608.

20. Wang, Y., Yuan, J., Zhang, X., Ling, X., Larson, B.W., Zhao, Q., Yang, Y., Shi, Y., Luther, J.M., and Ma, W. (2020). Surface ligand management aided by a secondary amine enables increased synthesis yield of CsPbI₃ perovskite quantum dots and high photovoltaic performance. Adv. Mater. *32*, e2000449.

21. Antony Jeyaseelan, A.A., and Dutta, S. (2015). Effect of ligand concentration on microstructure, ferroelectric and piezoelectric properties of PLZT film. Mater. Chem. Phys. *162*, 487–490.

22. Sun, Y., Pang, Z., Quan, Y., Han, D., Zhang, X., Ge, X., Wang, F., Sun, Y., Yang, J., and Yang, L. (2021). A synchronous defect passivation strategy for constructing high-performance and stable planar perovskite solar cells. Chem. Eng. J. *413*, 127387.

23. Sun, Y., Yang, S., Pang, Z., Quan, Y., Song, R., Chen, Y., Qi, W., Gao, Y., Wang, F., Zhang, X., et al. (2021). Preferred film orientation to achieve stable and efficient Sn-Pb binary perovskite solar cells. ACS Appl. Mater. Interfaces *13*, 10822–10836.

24. Djellabi, R., Yang, B., Wang, Y., Cui, X., and Zhao, X. (2019). Carbonaceous biomass-titania composites with Ti-O-C bonding bridge for efficient photocatalytic reduction of Cr(Vi) under narrow visible light. Chem. Eng. J. *366*, 172–180.

25. Jiang, Q., Zhao, Y., Zhang, X., Yang, X., Chen, Y., Chu, Z., Ye, Q., Li, X., Yin, Z., and You, J. (2019). Surface passivation of perovskite film for efficient solar cells. Nat. Photonics *13*, 460–466.

26. Kim, S.S., Kang, Y.S., Lee, H.D., Kim, J.K., and Hong, S.C. (2012). Physicochemical properties of chars at different treatment temperatures. J. Air Waste Manag. Assoc. *62*, 235–241.

27. Hwang, K., Kim, N., Jeong, Y., Sohn, H., and Yoon, S. (2021). Controlled nanostructure of a graphene nanosheet-TiO₂ composite fabricated via mediation of organic ligands for high-performance Li storage applications. Int. J. Energy Res. *45*, 16189–16203.

28. Iatsunskyi, I., Gottardi, G., Micheli, V., Canteri, R., Coy, E., and Bechelany, M. (2021). Atomic layer deposition of palladium coated TiO₂/Si nanopillars: ToF-SIMS, AES and XPS characterization study. Appl. Surf. Sci. *542*, 148603.

29. Li, F.N., Akhvlediani, R., Kuntumalla, M.K., and Hoffman, A. (2019). Oxygen bonding configurations and defects on differently oxidized diamond surfaces studied by high resolution electron energy loss spectroscopy and X-ray photoelectron spectroscopy measurements. Appl. Surf. Sci. *465*, 313–319.

30. Chowdhury, I.H., Kundu, S., and Naskar, M.K. (2018). Effect of organic acids on the physicochemical properties of titania and its photodegradation efficiency of methyl orange. J. Phys. Chem. Solids *121*, 367–374.

31. Zhang, Y., Liu, X., Li, P., Duan, Y., Hu, X., Li, F., and Song, Y. (2019). Dopamine-crosslinked TiO_2/perovskite layer for efficient and photo-stable perovskite solar cells under full spectral continuous illumination. Nano Energy 56, 733–740.

32. Bakre, P.V., and Tilve, S.G. (2017). Dicarboxylic acids as soft templates for the sol-gel synthesis of mesoporous Nano TiO_2 with enhanced photocatalytic activity. ChemistrySelect 2, 7063–7072.

33. Yang, D., Yang, R., Wang, K., Wu, C., Zhu, X., Feng, J., Ren, X., Fang, G., Priya, S., and Liu, S.F. (2018). High efficiency planar-type perovskite solar cells with negligible hysteresis using EDTA-complexed SnO_2. Nat. Commun. 9, 3239.

34. Shen, L., Song, P., Zheng, L., Liu, K., Lin, K., Tian, W., Luo, Y., Tian, C., Xie, L., and Wei, Z. (2021). Perovskite-type stabilizer for efficient and stable formamidinium-based lead iodide perovskite solar cells. J. Mater. Chem. A 9, 20807–20815.

35. Chen, J., Zhao, X., Kim, S.-G., and Park, N.-G. (2019). Multifunctional chemical linker imidazoleacetic acid hydrochloride for 21% efficient and stable planar perovskite solar cells. Adv. Mater. 39, 1902902.

36. Sajid, S., Elseman, A.M., Ji, J., Dou, S., Wei, D., Huang, H., Cui, P., Xi, W., Chu, L., Li, Y., et al. (2018). Computational study of ternary devices: stable, low-cost, and efficient planar perovskite solar cells. Nano Micro Lett. 10, 51.

37. Yang, L., Feng, J., Liu, Z., Duan, Y., Zhan, S., Yang, S., He, K., Li, Y., Zhou, Y., Yuan, N., et al. (2022). Record-efficiency flexible perovskite solar cells enabled by multifunctional organic ions interface passivation. Adv. Mater. 34, e2201681.

38. Cao, Q., Li, Y., Zhang, H., Yang, J., Han, J., Xu, T., Wang, S., Wang, Z., Gao, B., Zhao, J., et al. (2021). Efficient and stable inverted perovskite solar cells with very high fill factors via incorporation of star-shaped polymer. Sci. Adv. 7, eabg0633.

39. Yang, B., Suo, J., Di Giacomo, F., Olthof, S., Bogachuk, D., Kim, Y., Sun, X., Wagner, L., Fu, F., Zakeeruddin, S.M., et al. (2021). Interfacial passivation engineering of perovskite solar cells with fill factor over 82% and outstanding operational stability on n-i-p Architecture. ACS Energy Lett. 6, 3916–3923.

40. He, J., Liu, J., Hou, Y., Wang, Y., Yang, S., and Yang, H.G. (2020). Surface chelation of cesium halide perovskite by dithiocarbamate for efficient and stable solar cells. Nat. Commun. 11, 4237.

41. Kresse, G., and Furthmüller, J. (1996). Efficiency of ab-initio total energy calculations for metals and semiconductors using a plane-wave basis set. Comput. Mater. Sci. 1, 15–50.

42. Kresse, G., and Furthmüller, J.J. (1996). Efficient iterative schemes for ab initio total-energy calculations using a plane-wave basis set. Phys. Rev. B Condens. Matter 54, 11169–11186.

43. Perdew, J.P., Burke, K., and Ernzerhof, M. (1996). Generalized gradient approximation made simple. Phys. Rev. Lett. 77, 3865–3868.

44. Dion, M., Rydberg, H., Schröder, E., Langreth, D.C., and Lundqvist, B.I. (2004). Van der Waals density functional for general geometries. Phys. Rev. Lett. 92, 246401.
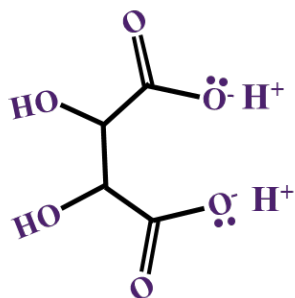
Supplemental information
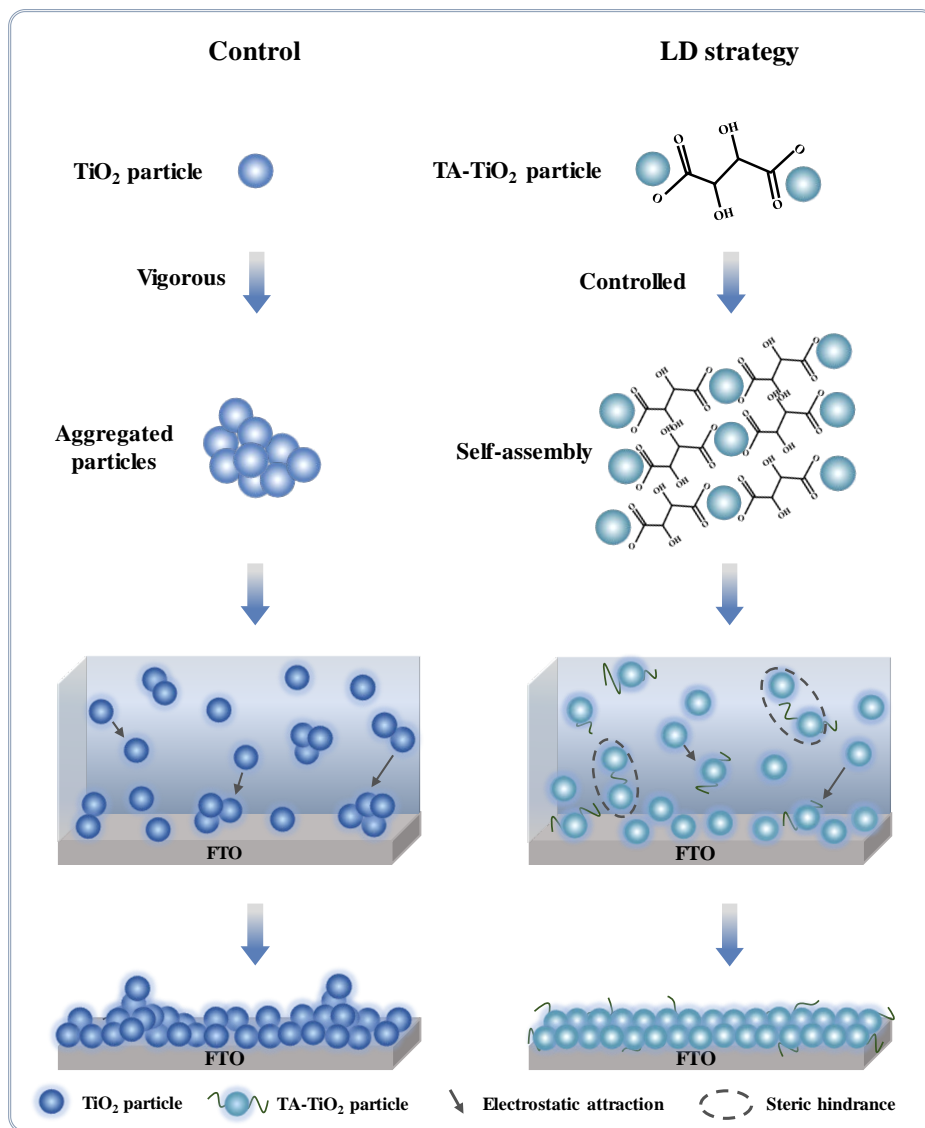
24.8%-efficient planar perovskite solar cells

via ligand-engineered TiO$_2$ deposition

Hao Huang, Peng Cui, Yan Chen, Luyao Yan, Xiaopeng Yue, Shujie Qu, Xinxin Wang, Shuxian Du, Benyu Liu, Qiang Zhang, Zhineng Lan, Yingying Yang, Jun Ji, Xing Zhao, Yingfeng Li, Xin Wang, Xunlei Ding, and Meicheng Li
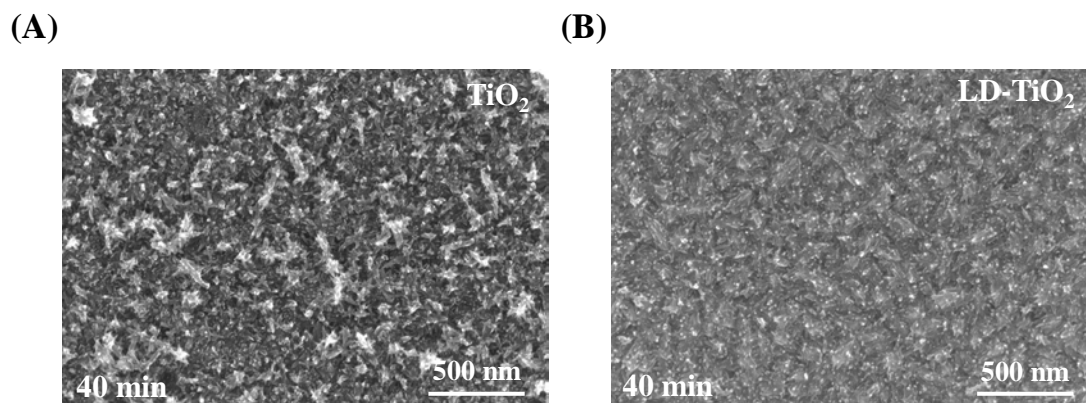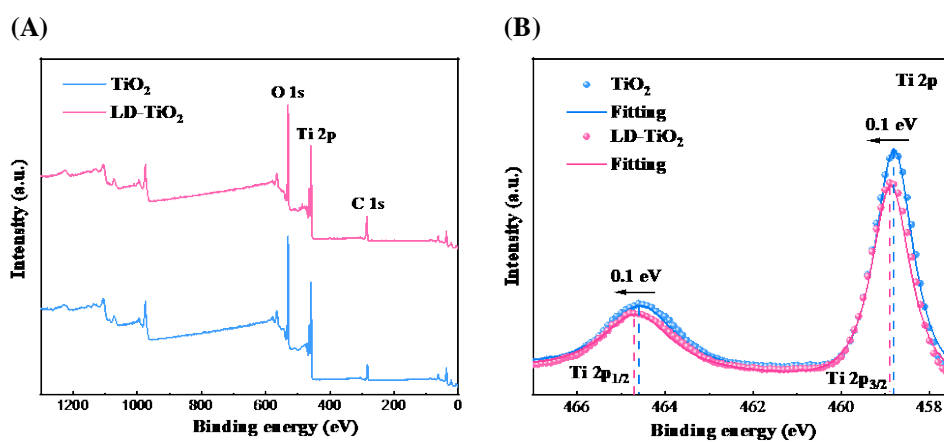
Supplemental figures:

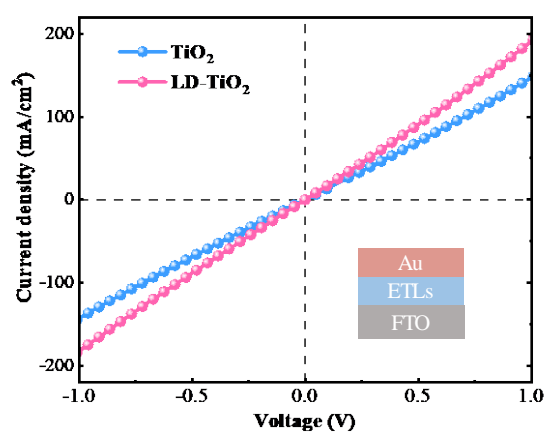**Figure S1.** Chemical structure of tartaric acid molecular.


Figure S2. Schematic of the chemical bath deposition process.

(A) **(B)**

**Figure S3.** SEM images of TiO₂ (A) and LD-TiO₂ film (B).

(A) **(B)**

Figure S4. XPS spectra of TiO₂ and LD-TiO₂ films, both films deposited on FTO. (A) Full XPS spectra of TiO₂ and LD-TiO₂ films. (B) The high-resolution spectra of Ti 2p.

Figure S5. Characterization of conductivity of TiO_2 and LD-TiO_2 films, the device structure for measurement is presented in the inset.
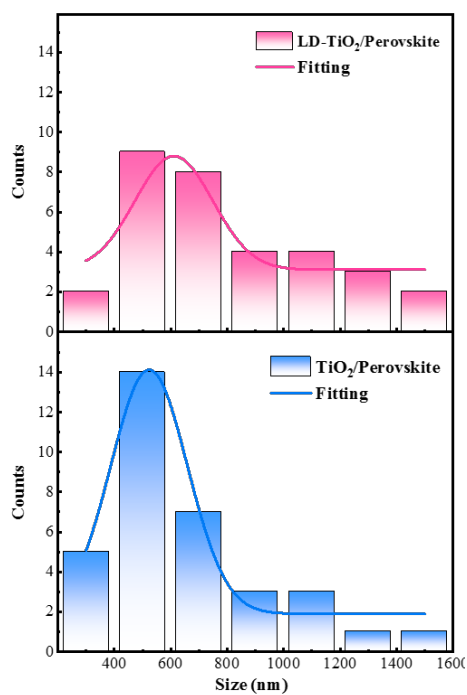

Figure S6. The grain size distribution of perovskite deposited on various substrates.

(A)   **(B)**

240 nm

-20 nm

TiO₂/perovskite   LD-TiO₂/perovskite
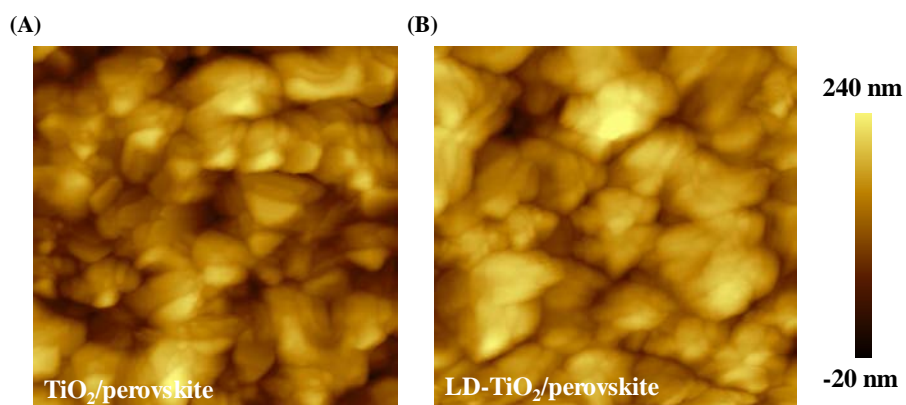
Figure S7. AFM images of perovskite films. (A) AFM images of perovskite film on TiO_2 film, the image size is 3 × 3 µm. (B) AFM images of perovskite film on LD-TiO_2 film, the image size is 3 × 3 µm.

Note S1. The AFM images description of perovskite films on TiO_2 and LD-TiO_2 films.

The grain size of perovskite film on LD-TiO_2 is slightly larger and more uniform, and all the grains distribute over the whole film neatly, resulting in a clear and continuous grain outline. In comparison, it is obviously to find that there are many of tiny grains overlap and distribute disorderly in the film on TiO_2.
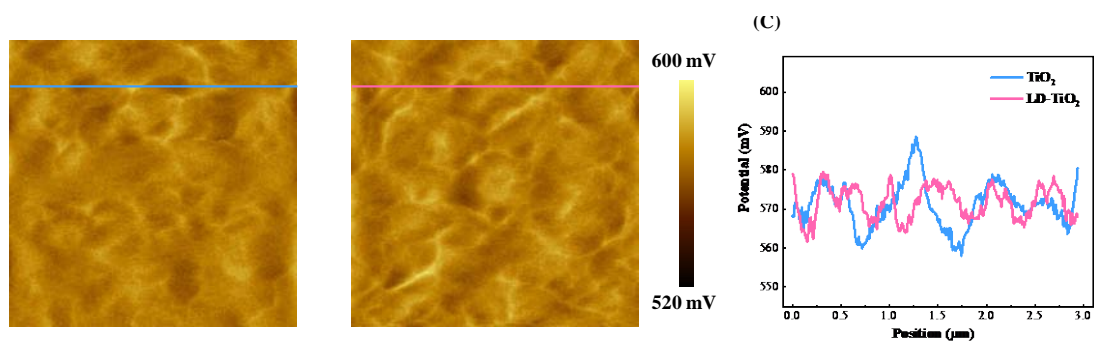
Figure S8. KPFM images of perovskite films. (A) KPFM images of perovskite film on TiO$_2$ film, the image size is 3 × 3 μm. (B) KPFM images of perovskite film on LD-TiO$_2$ film, the image size is 3 × 3 μm. (C) Surface potential line profiles of the corresponding perovskite films (the blue line in A and the pink line in B).

Note S2. The KPFM results description of perovskite films on TiO$_2$ and LD-TiO$_2$ films.

The KPFM results suggest that the LD deposition strategy has negligible impact on the fermi-level position of perovskite film. However, after analyzing the surface potential line profiles (Figure S8C) of the corresponding perovskite films, it is found that the potential fluctuation crossing the grains in perovskite on LD-TiO$_2$ is much smaller than that of perovskite on LD-TiO$_2$, indicating the decreased electron accumulation in the grain boundary.
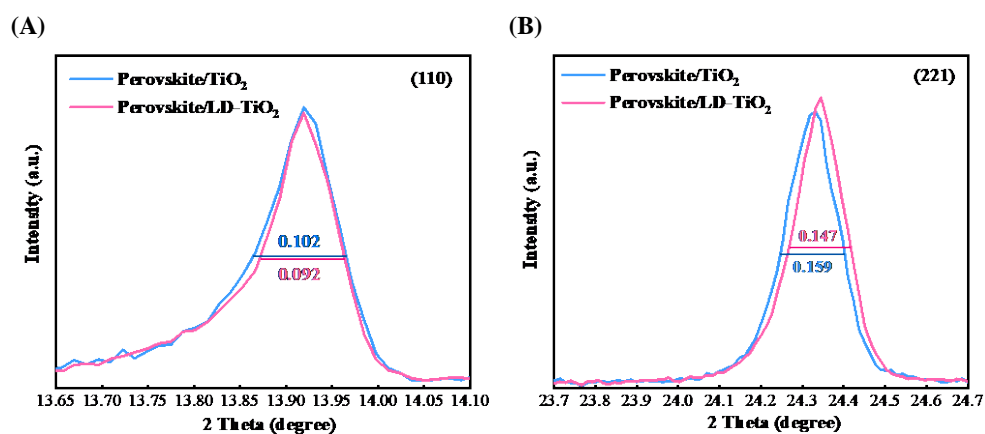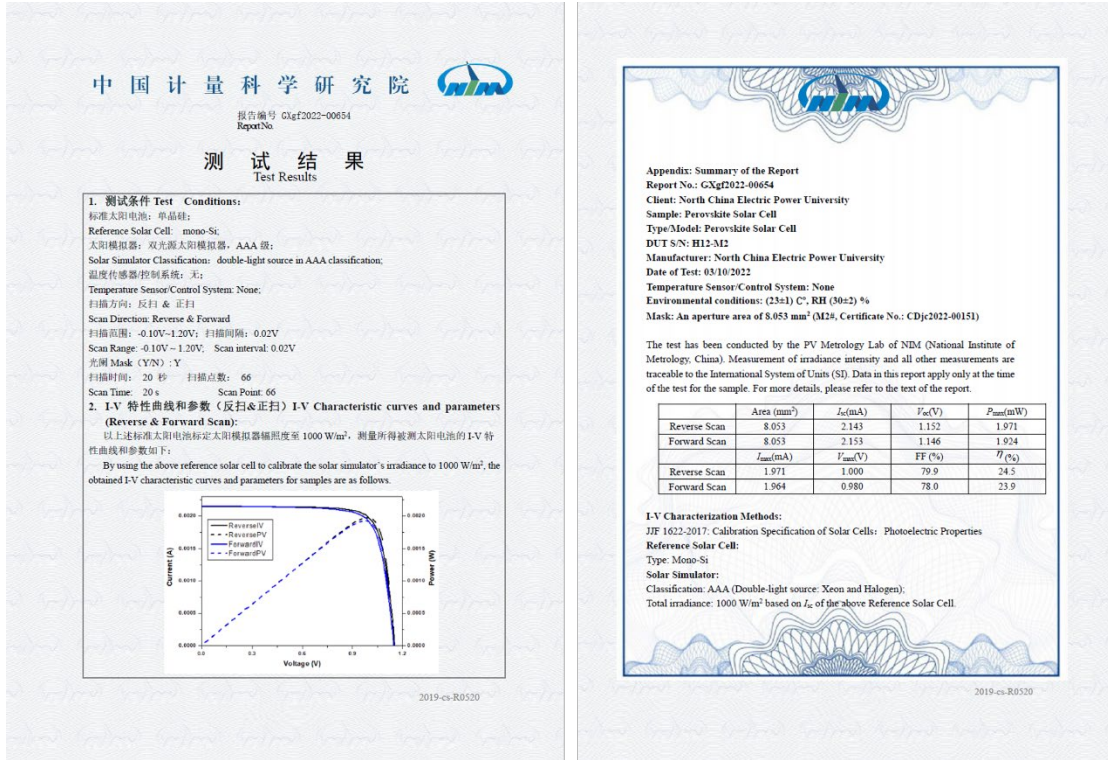
Figure S9. The crystallinity characterization of perovskite films on TiO$_2$ and LD-TiO$_2$ film. (A) FWHM of (110) face. (B) FWHM of (221) face.
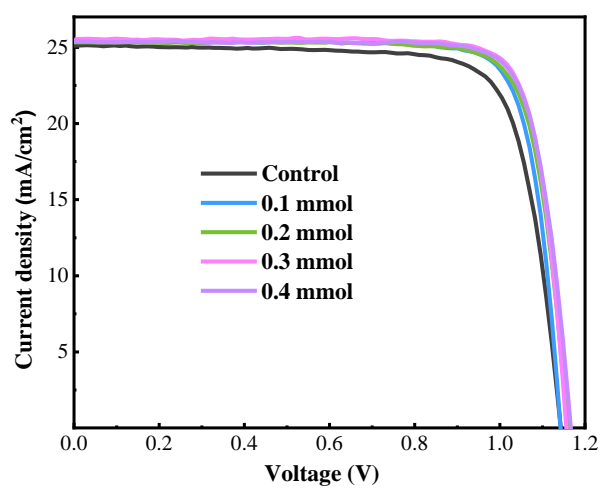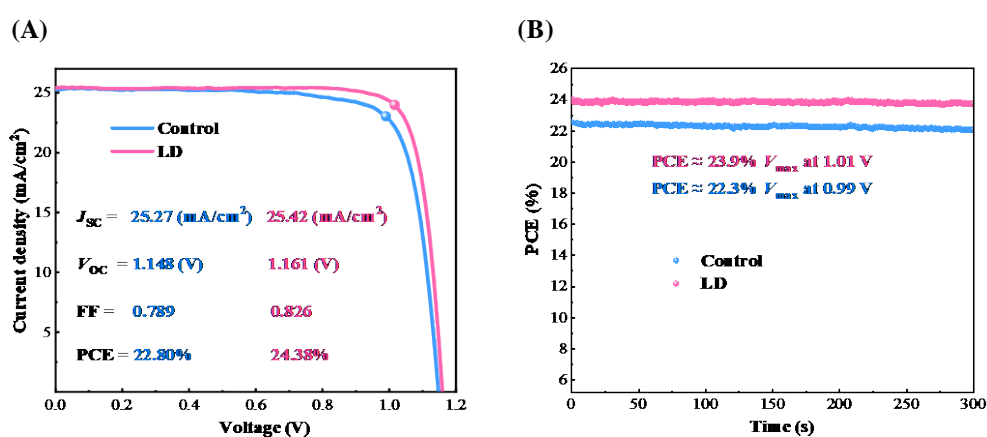

Figure S10. *J–V* curves (reverse scan) of planar PSCs with various ETLs, the used ETLs includes TiO$_2$, LD-TiO$_2$ with different TA concentration, the area of cell is 0.08053 cm^2.

Figure S11. Certificated results by the National Institute of Metrology, China (NIM, China). The planar PSC has been deposited an antireflective layer before measurement.
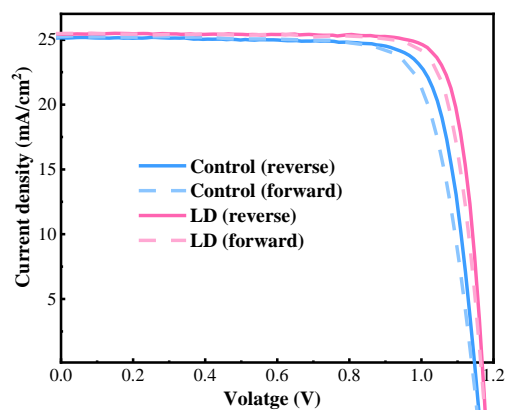
Figure S12. $J-V$ curves (reverse scan and forward scan) of planar PSC with TiO_2 and LD-TiO_2, the area of cell is 0.08053 cm^2.



Figure S13. Performance of the planar PSCs with various TiO_2 films. (A) $J-V$ curves (reverse scan) of planar PSCs with various ETLs, the area of the cell is 0.08053 cm^2. (B) Steady-state efficiency at the maximum power point for planar PSCs with various ETLs.

Note S3. The description of Steady-state efficiency at the maximum power point for planar PSCs with various TiO_2 films.

The planar PSCs with LD-TiO_2 exhibits a PCE of 24.38% which is superior to that of the control PSCs. Among the photovoltaic parameters, the FF of PSCs with LD-TiO_2 also exhibits an obvious improvement from 0.789 to 0.826. Importantly, the stabilized PCE of PSCs with LD-TiO_2 is ~23.9%, the stabilized PCE of the control device is ~22.3%, and both the PSCs exhibits a good output stability.
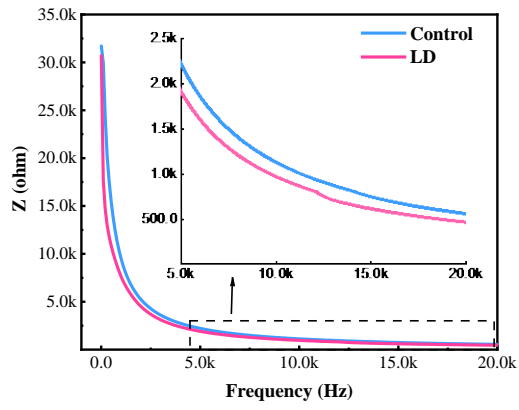
Figure S14. Impedance evolution verse the frequency of planar PSCs with various ETLs, devices structured as FTO/TiO$_2$ (LD-TiO$_2$)/ FA$_{0.92}$MA$_{0.08}$PbI$_3$/Spiro/Au.
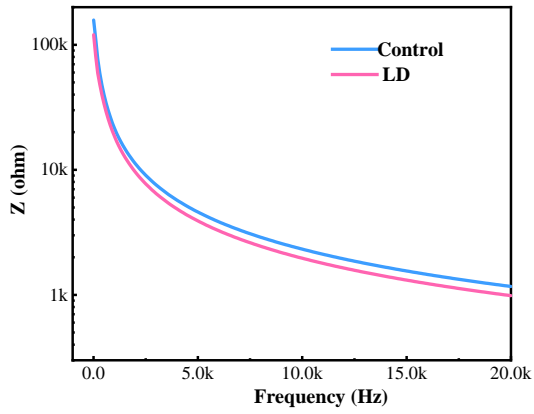
Figure S15. Impedance evolution verse frequency of devices structured as FTO/TiO$_2$ (LD-TiO$_2$)/ FA$_{0.92}$MA$_{0.08}$PbI$_3$/Au.
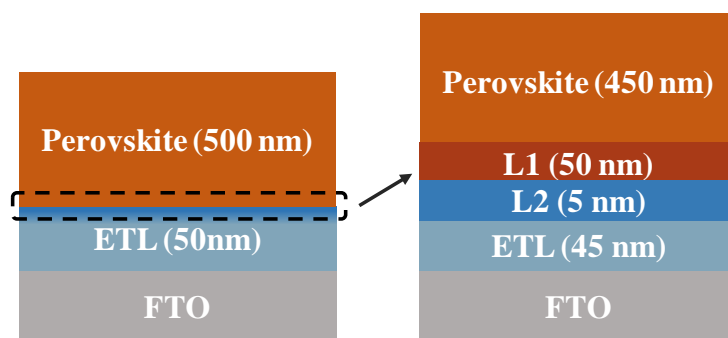
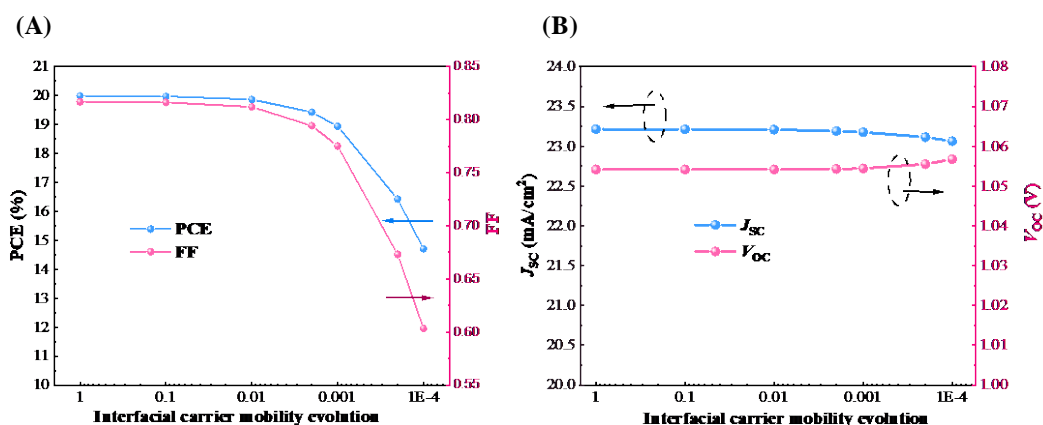**Figure S16.** Schematic illustration of device structure for simulation using wxAMPS. We split the ETL into two parts: one was the ETL that is 45 nm and another is the interfacial ETL that is 5 nm named as L2. The operation on perovskite layer is the same with that of ETL, and the interfacial perovskite layer is named as L1.

Figure S17. Photovoltaic parameters evolution verse interfacial impedance, the parameters for wxAMPS calculation are shown in Table S8. (A) Photovoltaic parameters (PCE and FF) evolution verse interfacial impedance researched by wxAMPS Simulation. (B) Photovoltaic parameters (J_{SC} and V_{OC}) evolution verse interfacial impedance researched by wxAMPS simulation.
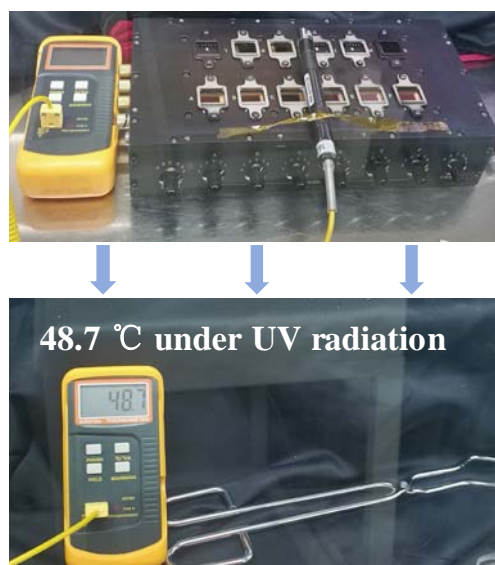
Figure S18. The equipment for UV stability test.
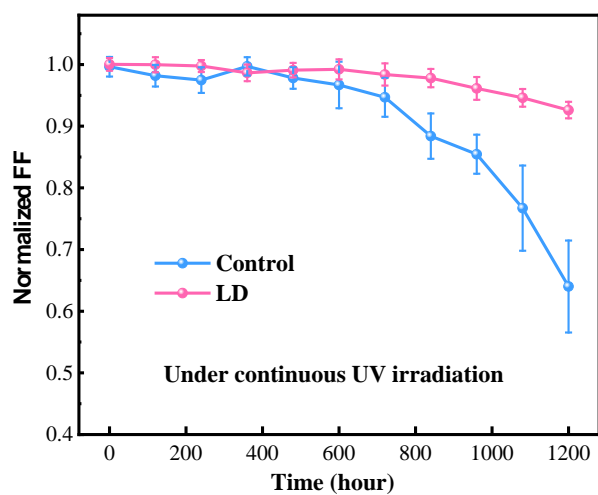
Figure S19. The evolution of FF. The unencapsulated PSCs with TiO_2 and $LD-TiO_2$ are under continuous 254 nm UV irradiation with an intensity of 50 mW/cm^2 at glove box filled N_2. 10 individuals are included in the stability test.
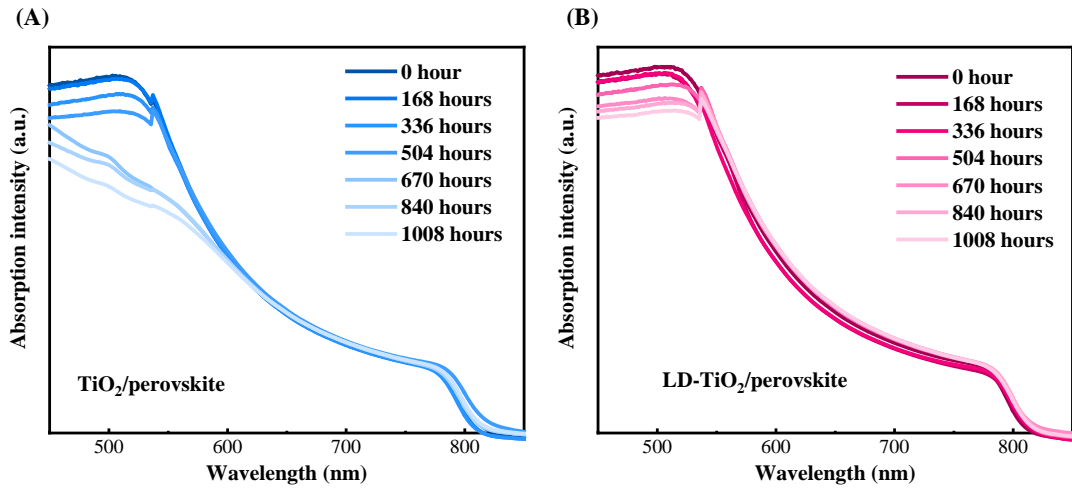
Figure S20. Absorption spectra of perovskite film on various TiO$_2$ film with different UV irradiation time. (A) Absorption spectra of perovskite film on TiO$_2$. (B) Absorption spectra of perovskite film on LD-TiO$_2$. Both the samples structured as FTO/TiO$_2$ (LD-TiO$_2$)/perovskite are under continuous 254 nm UV irradiation with an intensity of 50 mW/cm^2, and the UV light incident direction is from FTO side.
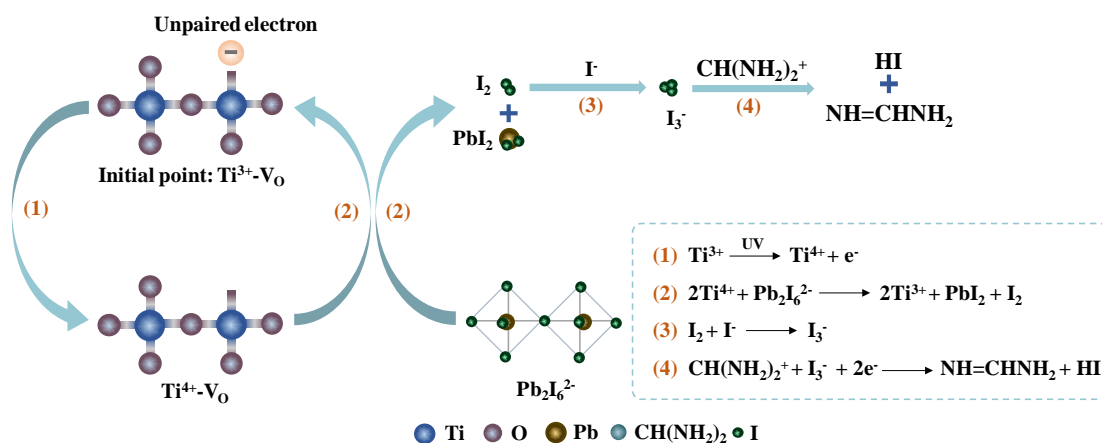
Figure S21. Degradation mechanism of PSCs under continuous UV irradiation.
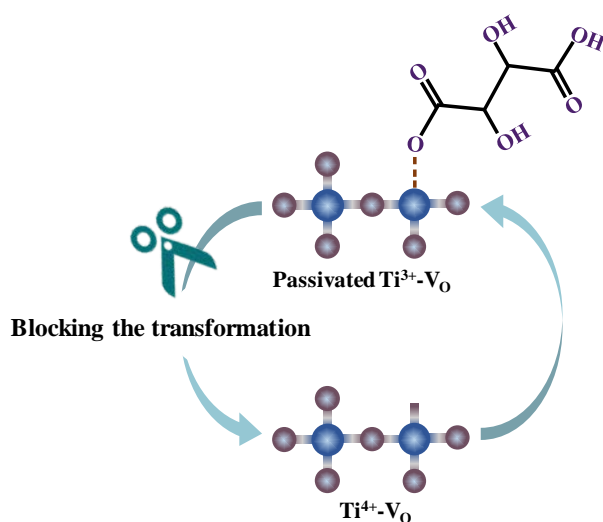
Figure S22. Passivation mechanism of tartaric acid on Ti^{3+}-V_O.

Note S4. The mechanism description of improved UV stability with LD strategy.

The Ti^{3+}-V_O defects play a key role in the performance decay of TiO_2-based PSCs under continuous UV irradiation. It is reported that the Ti^{3+}-V_O defects (oxygen vacancy) tend to convert into Ti^{4+}-V_O defects through the transition of unpaired electrons to valence band under the UV excitation. The Ti^{4+}-V_O with a deep trap level can capture photo-electrons, resulting in the degradation of the device performance. On the other hand, the Ti^{4+}-V_O defects can provide a mass of oxidizing sites, resulting in the decomposition of perovskite materials.[1-3] As seen in Figure S20, the I^- of the $Pb_2I_6^{2-}$ can be oxidized to I_2 by Ti^{4+}-V_O, leading to the collapse of the $Pb_2I_6^{2-}$ octahedral structure. Furthermore, the generated I_2 will combine with the free I^- reversibly (free I^- is abundant in perovskite material[4-6]), producing polyiodide species I_3^- with strong reduction.[7] According to the Pearson hard and soft acid base concept,[7,8] the neutralization reaction of free soft acid $CH(NH_2)_2^+$ and free soft base I_3^- happens spontaneously with the participation of photoelectrons. This process generates humidity labile $NH=CHNH_2$ and HI, and

exposes PbI_2 product, resulting in the perovskite decomposition. Hence, the passivation of Ti^{3+}-V_O defects is the fundamental approach to improve the device's UV stability.

Ligand-engineered deposition (LD) strategy can passivate Ti^{3+}-V_O defects in TiO_2 layer and improves the device's UV stability. The introduced ligand, such as tartaric acid, can coordinate with in Ti^{3+}-V_O due to lone pair electrons to block the transformation of oxidizing Ti^{4+}-V_O, as shown in Figure S21. Therefore, LD strategy can not only reduce the recombination loss of photo-electrons under UV excitation, but also inhibit the decomposition of perovskite material, decreasing the adverse influence of TiO_2 on device performance under continuous UV irradiation.
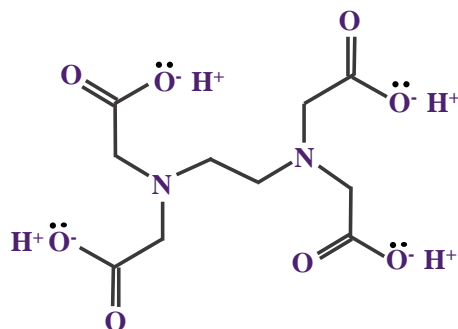
Figure S23. Chemical structure of EDTA molecular.
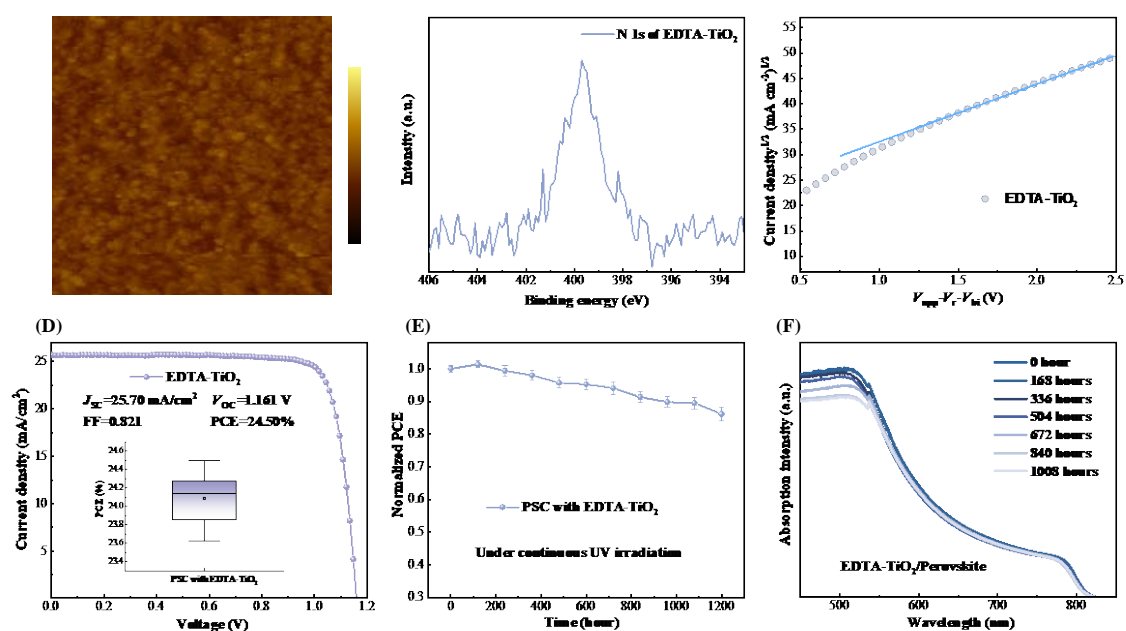
Figure S24. Effects of EDTA-TiO$_2$ on planar PSCs. (A) AFM images of EDTA-TiO$_2$ film. (B) XPS spectrum of EDTA-TiO$_2$ film. (C) Electron mobility measurement of EDTA-TiO$_2$ film (3.65×10^{-5} cm^{2}V^{-1}s^{-1}) using the SCLC model. (D) *J–V* curves (reverse scan) of the champion planar PSC with EDTA-TiO$_2$, the area of cell is 0.08053 cm^2. The distribution of PCEs (10 individuals) is presented in the inset. (E) The evolution of PCE. The unencapsulated 10 PSCs with EDAT-TiO$_2$ are under continuous 254-nm UV irradiation with an intensity of 50 mW/cm^2 at glove box filled N$_2$. After 1200 hours of continuous UV radiation, the PSCs with EDTA-TiO$_2$ can maintain ~86% of their initial PCE. (F) Absorption spectra of perovskite film deposited on EDTA-TiO$_2$ film. The sample structured as FTO/EDTA-TiO$_2$/perovskite is under continuous 254-nm UV irradiation with an intensity of 50 mW/cm^2, and the UV light incident direction is from FTO side. The absorption intensity of perovskite film on EDTA-TiO$_2$ shows good stability under continuous UV irradiation from the FTO side for 1008 hour.
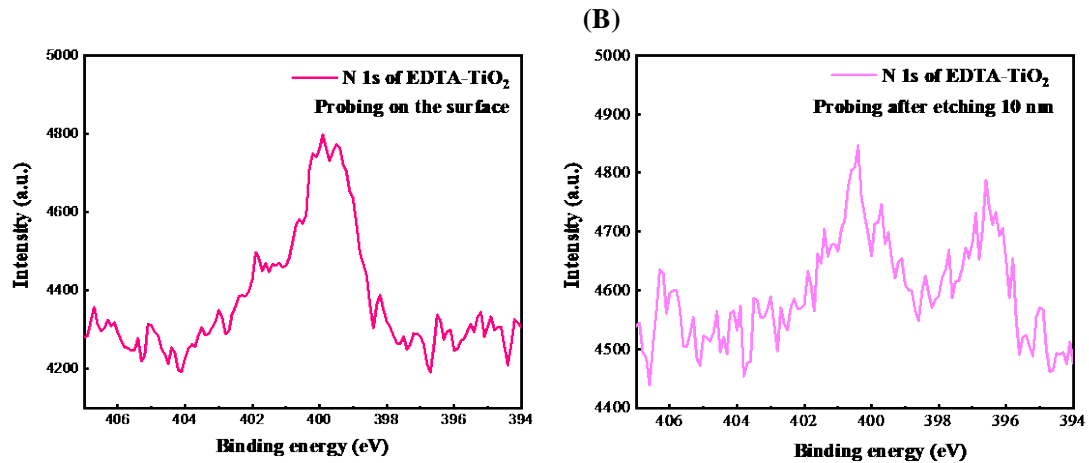
Figure S25. N 1s peak of LD-TiO$_2$ film with probing at different places. (A) N1s peak of LD-TiO$_2$ film with probing at the surface. (B) N1s peak of LD-TiO$_2$ film with probing after etching 10 nm.

Note S5. The description of depth dependent XPS results of EDTA-TiO$_2$ film.

To confirm the ligands not only locate on the surface of TiO$_2$, we performed the depth dependent XPS measurement. In the experiment, the ligand is EDTA due to the existed N elements. As shown in the Figure S25, after 10 nm etched, we can still characterize the existence of EDTA, indicating the ligands can distribute in the bulk of LD-TiO$_2$ film.
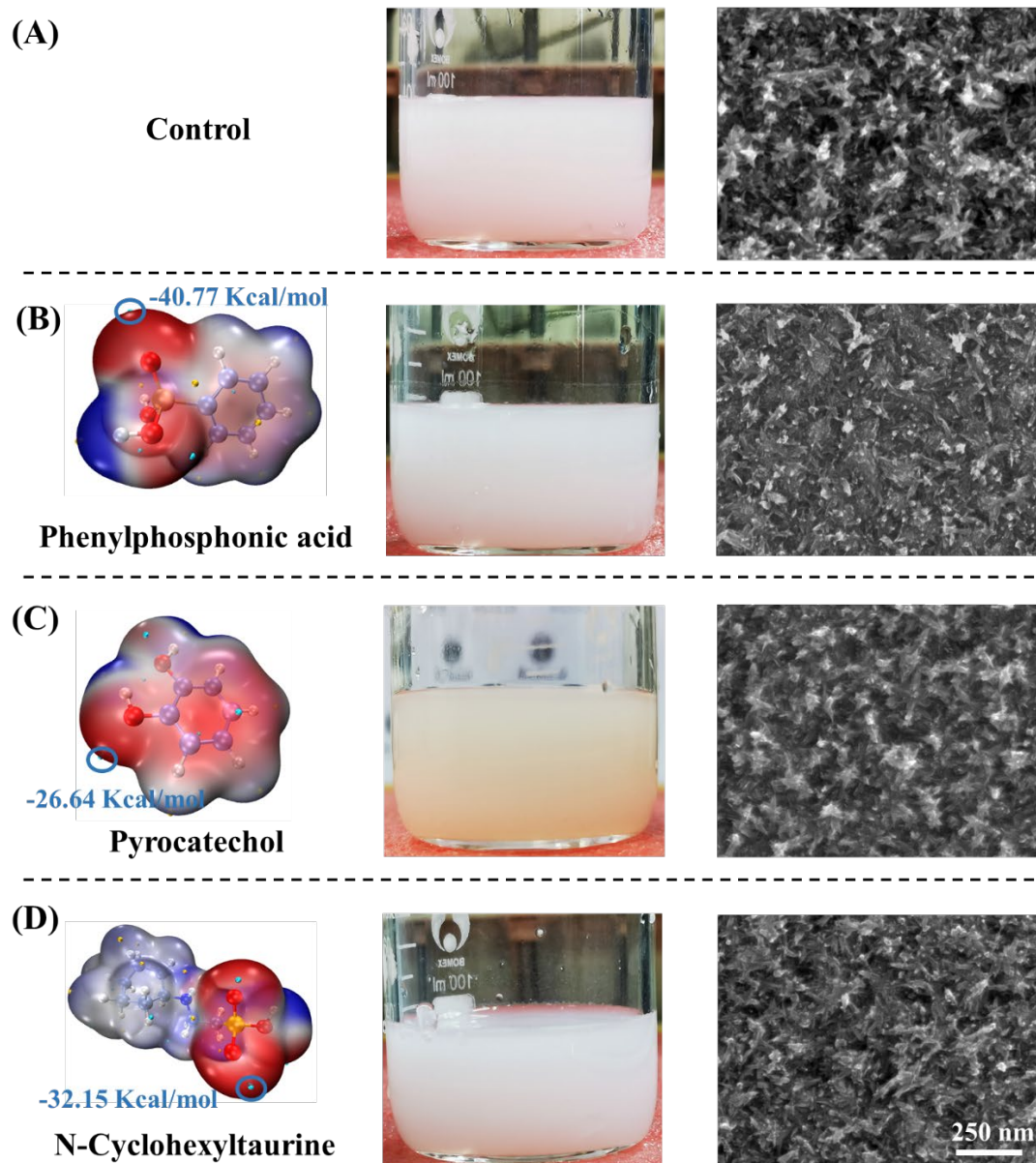
Figure 26. The Ligand-engineered strategy with different materials. (A) The optical photo of TiO$_2$ bath precursor, the SEM image of TiO$_2$ film. (B) Surface electrostatic potential of Phenylphosphonic acid (PA), the optical photo of PA-TiO$_2$ bath precursor, the SEM image of PA-TiO$_2$ film. (C) Surface electrostatic potential of Pyrocatechol (PY), the optical photo of PY-TiO$_2$ bath precursor, the SEM image of PY-TiO$_2$ film. (D) Surface electrostatic potential of N-Cyclohexyltaurine (NC), the optical photo of NC-TiO$_2$ bath precursor, the SEM image of NC-TiO$_2$ film.
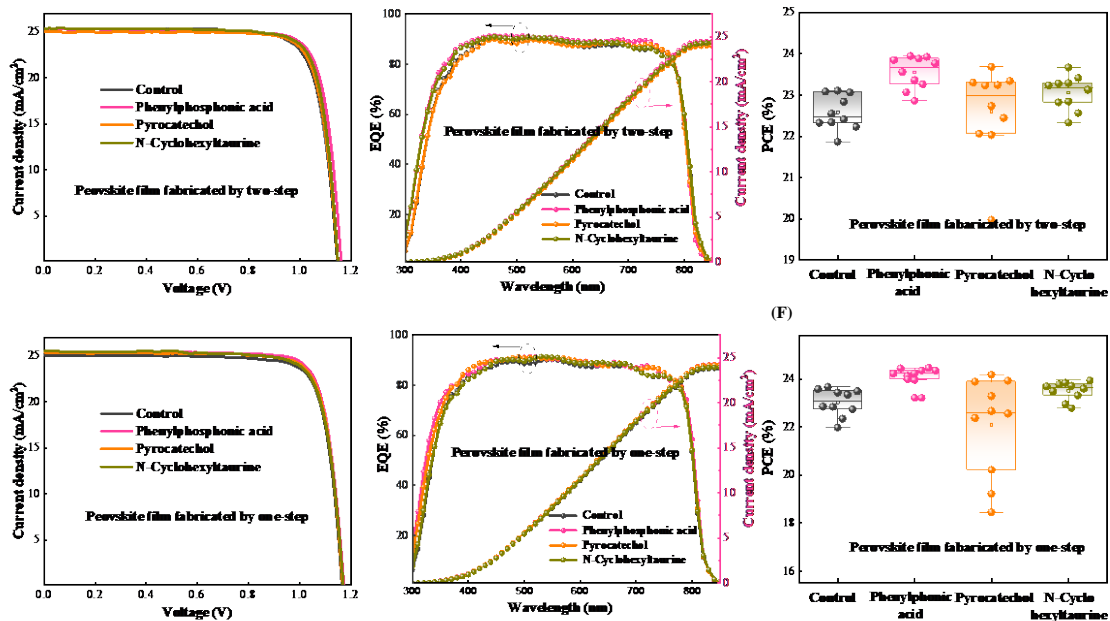
Figure S27. Performance of the planar PSCs with various TiO$_2$ films, the perovskite film is fabricated with the two-step method and one-step method. (A and D) *J–V* curves (reverse scan) of the champion planar PSCs with various ETLs, the area of the cell is 0.08053 cm^2. (B and E) The corresponding EQE and integrated current density curves of planar PSCs with various ETLs. (C and F) Statistical results of PCEs (reverse scan) fitted from 10 planar PSCs with various ETLs.

Note S6. The analysis of LD strategy extension using PA, PY and NC as the ligands.

The surface electrostatic potential suggests that all these materials presented in Figure S25 exhibit coordination ability due to their lone-pair electrons. In detail, the coordination ability of PA is supposed to be stronger than that of the PY and NC, resulting from the strong nucleophilicity of -PO$_3$H$_2$ group. After involving the additive into the water and preparing the bath precursor, the color of PY-TiO$_2$ bath precursor turns into orange, which would have some impacts on the deposited TiO$_2$ film.

Through the SEM characterization, we find that the ligand-engineered deposition strategy with different materials can have a positive effect on the aggregation inhibition. In comparison, the PA-TiO$_2$ exhibits a more compact and smoother surface, which may result from his strong coordination ability. It is noted that after the chemical bath deposition, the PY-TiO$_2$ exhibits a serious segregation, leading to an obvious ununiformly distribution at centimeter scale which can be observed with human eyes. The PY-TiO$_2$ segregation is supposed to decrease the performance of PY-TiO$_2$ based PSCs, especially its repeatability. The molecular sizes of PA, PY and NC are also calculated with the results shown in Table S9, the PY molecular possesses a smaller size in the c-axis direction, which may not be conducive to inhibit particle aggregation.

We further fabricated the perovskite films on different TiO$_2$ substrates by the two-step method and one-step method, then explored the influence of introduced materials on the performance of planar PSCs. Although the PSCs with PY-TiO$_2$ exhibited a bad repeatability, the

champion PCE and average PCE of PSCs have been effectively improved after regulation with LD strategy using all these ligands compared to control device, indicating that the ligand-engineered deposition strategy exhibit an excellent reliability and broad applicability. (Figure S26 and Table S10)

Basing the on above analysis, we can find that the ligand-engineered deposition strategy exhibits an excellent reliability and broad applicability. For choosing suitable ligand to obtain an ideal effect, the coordination ability, number and distribution of coordination groups, molecular configuration and size of these material should be comprehensively considered.

Supplemental tables:

Table S1. The statistic parameters of planar PSCs with different amount of TA

	J_{SC} (mA/cm^2)	V_{OC} (V)	FF	PCE (%)
Control	25.11	1.148	0.774	22.30
0.1 mmol	25.43	1.148	0.81	23.64
0.2 mmol	25.33	1.161	0.809	23.79
0.3 mmol	25.55	1.161	0.82	24.32
0.4 mmol	25.39	1.161	0.819	24.15

Table S2. The statistic parameters of champion planar PSC with reverse and forward scan, the hysteresis is calculated according to the equation of hysteresis=(R_{PCE}-F_{PCE})/R_{PCE}.

	J_{SC} (mA/cm^2)	V_{OC} (V)	FF	PCE (%)	Hysteresis
Control (R)	25.15	1.148	0.798	23.04	3.52%
Control (F)	25.23	1.135	0.776	22.22	
LD (R)	25.43	1.174	0.831	24.81	2.46%
LD (F)	25.48	1.161	0.817	24.18	

Table S3. The statistic parameters of 40 planar PSCs with TiO_2

	J_{SC} (mA/cm^2)	V_{OC} (V)	FF	PCE (%)
1	24.98	1.122	0.787	22.06
2	24.91	1.109	0.777	21.46
3	25.23	1.135	0.776	22.22
4	24.82	1.122	0.789	21.98
5	25.07	1.135	0.777	22.09
6	25.15	1.147	0.798	23.04
7	24.78	1.122	0.804	22.36
8	24.93	1.109	0.802	22.18
9	24.88	1.109	0.788	21.73
10	25.22	1.122	0.799	22.61
11	25.12	1.122	0.803	22.64
12	24.82	1.148	0.784	22.32
13	25.20	1.122	0.787	22.24
14	25.13	1.122	0.8	22.57
15	24.89	1.122	0.785	21.92
16	24.91	1.135	0.797	22.52
17	25.00	1.122	0.8	22.45
18	25.02	1.135	0.785	22.29
19	24.99	1.131	0.802	22.66
20	25.29	1.109	0.806	22.62
21	25.12	1.135	0.795	22.67
22	24.99	1.144	0.796	22.76
23	24.89	1.126	0.778	21.81
24	24.95	1.118	0.779	21.74
25	25.03	1.109	0.807	22.39
26	25.21	1.122	0.793	22.42
27	25.13	1.109	0.807	22.48
28	24.93	1.135	0.789	22.32
29	24.99	1.122	0.805	22.58
30	24.68	1.122	0.799	22.14
31	24.90	1.135	0.79	22.32
32	24.90	1.135	0.789	22.29
33	24.68	1.148	0.803	22.77
34	25.08	1.148	0.781	22.47
35	25.01	1.140	0.805	22.96
36	24.98	1.140	0.768	21.86
37	25.18	1.100	0.787	21.80
38	24.54	1.135	0.785	21.85
39	24.56	1.135	0.786	21.92
40	24.97	1.135	0.776	22.00

Table S4. The statistic parameters of 40 planar PSCs with LD-TiO$_2$

	J_{SC} (mA/cm^2)	V_{OC} (V)	FF	PCE (%)
1	25.59	1.148	0.812	23.86
2	25.56	1.148	0.816	23.93
3	25.43	1.135	0.835	24.09
4	25.67	1.161	0.809	24.11
5	25.72	1.161	0.816	24.37
6	25.43	1.174	0.831	24.81
7	25.64	1.161	0.81	24.11
8	25.53	1.161	0.805	23.85
9	25.43	1.161	0.828	24.42
10	25.57	1.122	0.834	23.93
11	25.51	1.135	0.831	24.06
12	25.43	1.187	0.813	24.55
13	25.29	1.122	0.834	23.68
14	25.35	1.161	0.823	24.21
15	25.49	1.161	0.828	24.51
16	25.47	1.148	0.83	24.25
17	25.56	1.148	0.821	24.08
18	25.49	1.135	0.827	23.93
19	25.69	1.135	0.833	24.29
20	25.52	1.148	0.826	24.19
21	25.38	1.148	0.825	24.05
22	25.48	1.135	0.822	23.77
23	25.32	1.122	0.825	23.42
24	25.59	1.148	0.821	24.10
25	25.43	1.148	0.821	23.96
26	25.55	1.161	0.824	24.43
27	25.49	1.161	0.821	24.31
28	25.61	1.161	0.822	24.41
29	25.30	1.161	0.822	24.12
30	25.41	1.161	0.827	24.40
31	25.83	1.174	0.81	24.56
32	25.61	1.161	0.827	24.59
33	25.59	1.148	0.831	24.40
34	25.44	1.148	0.829	24.19
35	25.61	1.161	0.822	24.42
36	25.43	1.174	0.815	24.32
37	25.46	1.174	0.819	24.46
38	25.48	1.174	0.818	24.48
39	25.55	1.187	0.815	24.71
40	25.45	1.161	0.825	24.37

Table S5. A List of reported representative PCE of planar PSCs with TiO_2 as ETL

Structure	Method of TiO_2 film	PCE (%)	Year	Reference
$ITO/TiO_2/Cs_xFA_{1-x}PbI_3$	Spin coating	22.1	2018	9
$ITO/TiO_2/Cs_{0.1}FA_{0.78}MA_{0.12}PbI_{2.55}Br_{0.45}$	Spin coating	22.3	2019	10
$FTO/TiO_2/Cs_{0.08}FA_{0.92}PbI_3$	Chemical bath deposition	23.25	2020	11
$ITO/NaCl-TiO_2/FA_{0.92}MA_{0.08}PbI_3$	Spin coating	23.15	2021	12
$FTO/TiO_2/Cs_{0.05}FA_{0.85}MA_{0.1}PbI_{2.91}Br_{0.09}$	Chemical bath deposition	23.4	2021	13
$FTO/TiO_2\&PCBA/FA_{0.97}Cs_{0.03}PbI_{2.91}Br_{0.09}$	Spin coating	24.25	2022	14
$FTO/LD-TiO_2/FA_{0.92}MA_{0.08}PbI_3$	Ligand-engineered deposition	24.81	2022	This work

Table S6. A list of reported representative PCE of perovskite solar cells that fabricated with a two-step method

Structure	PCE (%)	Year	Annotation
ITO/SnO$_2$/(FAPbI$_3$)$_x$(MAPbI$_3$)$_y$	23.6	2019	15
FTO/SnO$_2$/(FAPbI$_3$)$_x$(MAPbBr$_3$)$_y$	23.5	2020	16
ITO/SnO$_2$/(FAPbI$_3$)	24.1	2021	17
ITO/SnO$_2$/FA$_{1-x-y}$MA$_x$Cs$_y$PbI$_{3-z}$Br$_z$	24.27	2021	18
ITO/SnO$_2$/(FAPbI$_3$)$_x$(MAPbI$_3$)$_y$	24.4	2021	19
FTO/LD-TiO$_2$/FA$_{0.92}$MA$_{0.08}$PbI$_3$	24.81	2022	This work

Table S7. The statistic parameters of EIS fitting

Device	R_s (ohm/cm^2)	R_{co} (ohm/cm^2)	CPE1-T (F)	CPE1-P (F)	R_{re} (ohm/cm^2)	CPE2-T (F)	CPE2-P (F)
Control	24	216133	1.14E-7	0.94	631246	1.56E-4	0.68
Error%	1.5465	0.8351	3.6913	0.4167	13.75	4.2338	4.1525
LD	17.33	166546	1.26E-7	0.93	6440266	1.23E-5	0.83
Error%	1.1326	1.0156	3.4324	0.3403	4.7619	1.8396	0.8807

Note S7. The description of EIS fitting.

To explore the interface carrier transport characteristics of PSCs, when selecting the fitting circuit, it is necessary to comprehensively consider the shape of the tested spectra and the physical property of solar cells. In our experiments, it is noticed that the spectra included a completed semicircle and an unfinished semicircle. It is reported that the semicircle located in the high-frequency region is responding to impedance (R_{ct}) arising from the charge transport between the electron (hole) transport layer with the perovskite layer, and the semicircle located in the low-frequency region is associated with the carrier recombination impedance (R_{re}). Basing on above thinking and extensive literature research, a commonly used equivalent circuit was chosen in this fitting process. In the equivalent circuit, a pure resistor and a pseudo capacitor element are connected in parallel to describe a semicircle. Here, the constant phase angle element (CPE) defined by two parameters (CPE-T and CPE-P) is applied to represent the capacitive effect in the PSCs. Generally speaking, the value of CPE-P is between the 0.5~1, when it is 1, indicating the electronic component is a pure capacitor. In the fitting process, the value of CPE-P can describe the shape of semicircle, when the semicircle deviates to the X axis, it is supposed to be smaller. However, the value of CPE-P has slightly influence on the values of fitted Rre and Rct, which we are concerned about.

Table S8. The parameters for wxAMPS calculation

Parameters and units	Compact TiO$_2$	CH$_3$NH$_3$PbI$_3$	Spiro
ε_r	100	25	3
E_g (eV)	3.2	1.55	2.91
χ (eV)	4	3.93	2.2
Thickness (nm)	50	500	200
Electron and Hole mobility (cm^2/V S)	0.006	10	0.001
N_a (cm^{-3})	0	0	1×10^{18}
N_d (cm^{-3})	5×10^{19}	0	0
N_c (cm^{-3})	1×10^{21}	2.5×10^{20}	1×10^{18}
N_v (cm^{-3})	2×10^{20}	2.5×10^{20}	1×10^{18}

Table S9. The statistic parameters of TRPL measurement (light incident from FTO side)

Sample	τ_{ave}	τ_1	%	τ_2	%	R^2
FTO/TiO$_2$/perovskite	320.36	188.41	49.59	450.12	50.41	0.995
FTO/LD-TiO$_2$/perovskite	262.63	105.14	19.80	301.53	80.20	0.998

Note S8. The description of TRPL spectra fitting.

The TRPL spectra are fitted according to the function $I(t)=I_0+A_1\exp(-t/\tau_1) + A_2\exp(-t/\tau_2)$ and average time constant τ_{ave} is calculated using the $\tau_{ave}=(A_1*\tau_1^2+A_2*\tau_2^2)/(A_1*\tau_1+A_2*\tau_2)$.

Table S10. Molecular size of PA, PY and NC

Molecular size	PA	PY	NC
A (angstrom)	9.421	7.663	12.301
B (angstrom)	6.755	7.389	6.683
C (angstrom)	5.819	2.402	6.290

Table S11. Photovoltaic parameters (corresponding to Figure S26A and 26D)

	Perovskite fabrication method	J_{SC} (mA/cm^2)	V_{OC} (V)	FF	PCE (%)
Control	Two-step	25.37	1.148	0.794	23.11
	One-step	25.08	1.167	0.808	23.67
PA	Two-step	25.25	1.161	0.817	23.95
	One-step	25.41	1.174	0.82	24.46
PY	Two-step	25.25	1.154	0.813	23.68
	One-step	25.35	1.167	0.817	24.17
NC	Two-step	25.38	1.148	0.813	23.67
	One-step	25.52	1.167	0.804	23.94

Supplemental references:

1. Ji, J., Liu, X., Jiang, H., Duan, M., Liu, B., Huang, H., Wei, D., Li, Y. and Li, M. (2020). Two-stage ultraviolet degradation of perovskite solar cells induced by the oxygen vacancy-Ti^{4+} states. iScience *4*, 101013.

2. Ito, S., Tanaka, S., Manabe, K., and Nishino, H. (2014). Effects of surface blocking layer of Sb_2S_3 on nanocrystalline TiO_2 for $CH_3NH_3PbI_3$ perovskite solar cells. J. Phys. Chem. C *118*,16995–17000.

3. Shlenskaya, N.N., Belich, N.A., Gra¨tzel, M., Goodilin, E.A., and Tarasov, A.B. (2018). Light-induced reactivity of gold and hybrid perovskite as a new possible degradation mechanism in perovskite solar cells. J. Mater. Chem. A. *6*, 1780–1786.

4. Eames, C., Frost, J. M., Barnes, P. R., O'regan, B. C., Walsh, A., and Islam, M. S. (2015). Ionic transport in hybrid lead iodide perovskite solar cells. Nat. commun. *6*, 7497.

5. Haruyama, J., Sodeyama, K., Han, L., and Tateyama, Y. (2015). First-principles study of ion diffusion in perovskite solar cell sensitizers. J. Am. Chem. Soc. *137*, 10048-10051.

6. Azpiroz, J. M., Mosconi, E., Bisquert, J., and De Angelis, F. (2015). Defect migration in methylammonium lead iodide and its role in perovskite solar cell operation. Energy Environ. Sci. *8*, 2118-2127.

7. Shlenskaya, N. N., Belich, N. A., Grätzel, M., Goodilin, E. A., and Tarasov, A. B. (2018). Light-induced reactivity of gold and hybrid perovskite as a new possible degradation mechanism in perovskite solar cells. J. Mater. Chem. A *6*, 1780-1786.

8. Kim, S. H., Kim, E. M., Lee, C. M., Dong, W. K., Lim, S. T., Sohn, M. H., and Jeong, H. J. (2012). Synthesis of PEG-iodine-capped gold nanoparticles and their contrast enhancement in in vitro and in vivo for X-Ray/CT. J. Nanomater. *2012*, 344-353.

9. Li, Q., Zhao, Y., Fu, R., Zhou, W., Zhao, Y., Liu, X., Yu, D., and Zhao Q. (2018). Efficient perovskite solar cells fabricated through CsCl-enhanced PbI_2 precursor via sequential deposition. Adv. Mater. *30*, 1803095.

10. Zhao, Y., Li, Q., Zhou, W., Hou, Y., Zhao, Y., Fu, R., Yu, D., Liu, X., and Zhao Q. (2019). Double-side-passivated perovskite solar cells with ultra-low potential loss. Sol. RRL *3*, 1800296.

11. Zhu, X., Du, M., Feng, J., Wang, H., Xu, Z., Wang, L., Zuo, S., Wang, C., Wang, Z., Zhang, C., Ren, X., Priya, S., Yang, D. and Liu, S. F. (2020). High-efficiency perovskite solar cells with imidazolium-based ionic liquid for surface passivation and charge Transport. Angew. Chem. Int. Ed. Engl. *8*, 4238-4244.

12. Gao, F., Luo, C., Wang, X. and Zhao, Q. (2021). Alkali metal chloride-doped water-based TiO_2 for efficient and stable planar perovskite photovoltaics exceeding 23% efficiency. Small Methods *5*, 2100856.

13. Su, H., Zhang, J., Hu, Y., Du, X., Yang, Y., You, J., Gao, L. and Liu, S. (2021). Fluoroethylamine engineering for effective passivation to attain 23.4% efficiency perovskite solar cells with superior stability. Adv. Energy Mater. *11*. 2101454.

14. Li, Y., Chen, Z., Yu, B., Tan, S., Cui, Y., Wu, H., Luo, Y., Shi, J., Li, D. and Meng, Q. (2022). Efficient, stable formamidinium-cesium perovskite solar cells and minimodules enabled by crystallization regulation. Joule *3*, 676-689.

15. Jiang, Q., Zhao, Y., Zhang, X., Yang, X., Chen, Y., Chu, Z., Ye, Q., Li, X., Yin, Z. and You,

J. (2019). Surface passivation of perovskite film for efficient solar cells. Nat. Photonics *7*, 460-466.

16. Qin, M., Xue, H., Zhang, H., Hu, H., Liu, K., Li, Y., Qin, Z., Ma, J., Zhu, H., Yan, K., Fang, G., Li, G., Jeng, U-Ser, Brocks, G., Tao, S. and Lu, X. (2020). Precise control of perovskite crystallization kinetics via sequential A-site doping. Adv. Meter. *32*, 2004630.

17. Hui, W., Chao, L., Lu, H., Xia, F., Wei, Q., Su, Z., Niu, T., Tao, L., Du., B., Li, D., Wang, Y., Dong, H., Zuo, S., Li, B., Shi, W., Ran, X., Li, P., Zhang, H., Wu, Z., Ran, C., Song, L., Xing, G., Gao, X., Zhang, J., Xia, Y., Chen, Y., Huang, W. (2021). Stabilizing black-phase formamidinium perovskite formation at room temperature and high humidity. Science *371*, 1359-1364.

18. Li, N., Niu, X., Li, L., Wang, H., Huang, Z., Zhang, Y., Chen, Y., Zhang, X., Zhu, C., Zai, H., Bai, Y., Ma, S., Liu, H., Liu, X., Guo, Z., Liu, G., Fan, R., Chen, H., Wang, J., Lun, Y., Wang, X., Hong, J., Xie, H., Jakob, D.S., Xu, X.G., Chen, Q., Zhou, H. (2021). Liquid medium annealing for fabricating durable perovskite solar cells with improved reproducibility. Science *373*, 561-567.

19. Xiong, Z., Chen, X., Zhang, B., Odunmbaku, G. O., Ou, Z. Guo, B., Yang, K., Kan, Z., Lu, S., Chen, S., Ouedraogo, N. A. N., Cho, Y., Yang, C., Chen, J., Sun, K. (2021). Simultaneous interfacial modification and crystallization control by biguanide hydrochloride for stable perovskite solar cell with PCE of 24.4%. Adv. Mater. *34*, 2106118.